On the stochastic significance of peaks in the least-squares wavelet spectrogram and an application in GNSS time series analysis

Ebrahim Ghaderpour [a],[*], Spiros D. Pagiatakis [b], Gabriele Scarascia Mugnozza [a], Paolo Mazzanti [a]

[a] Department of Earth Sciences & CERI Research Center, Sapienza University of Rome, P.le Aldo Moro, 5, Rome, RM, 00185, Italy
[b] Department of Earth and Space Science and Engineering, York University, 4700 Keele St, Toronto, ON, M3J 1P3, Canada

ARTICLE INFO

ABSTRACT

In this paper, the mathematical derivation of the underlying probability distribution function for the normalized least-squares wavelet spectrogram is presented. The impact of empirical and statistical weights on the estimation of the spectral peaks and their significance are demonstrated from the statistical point of view both theoretically and practically. The simulation results show an improvement of approximately 0.02 mm (RMSE) for annual signal estimation when statistical weights are considered in the least-squares wavelet analysis (LSWA). The weighted LSWA estimates the signals more accurately than the ordinary LSWA for different percentage amount of missing data. As a real-world application, Global Navigation Satellite Systems (GNSS) time series for a station in Rome, Italy are analyzed. The analyses of the GNSS time series provided by different agencies for the same station reveal statistically significant annual peaks, more significant in 2010 but less significant between 2018 and 2020, while the higher frequency components show different spectral patterns over time. A declining trend of approximately −0.42 mm/year since 2004 is estimated for the GNSS height time series, likely due to gradual land subsidence. The results not only highlight the advantages of LSWA but can also help to better understand the uncertainties involved in signal estimation.

1. Introduction

Vaníček proposed the least-squares spectral analysis (LSSA) as an alternative to traditional discrete Fourier transform (DFT) [1–3]. The LSSA estimates a least-squares spectrum (LSS) for a given set of frequencies by fitting the sine waveforms to the time series while accounting for discontinuities or jumps [4]. The LSSA has advantages over DFT. First, LSSA can analyze unequally spaced (unevenly spaced or irregularly sampled) time series without any data aggregation including interpolation or gap-filling. Second, LSSA can consider the covariance matrix associated with the time series and rigorously evaluate the stochastic significance of peaks in the LSS [5,6]. Realizing that many time series in real-world applications, particularly in geoscience applications, are not regularly sampled and errors always exist in the measurements, LSSA has been widely accepted and applied to process such time series [7–9].

Following Vaníček's work, Ghaderpour and Pagiatakis proposed the least-squares wavelet analysis (LSWA), a robust extension of LSSA, which estimates a spectrogram instead of a spectrum [10]. The LSWA is an alternative to the traditional continuous wavelet transform (CWT) [3, 9,11]. Unlike LSSA that decomposes a time series into the frequency domain, LSWA decomposes the time series into the time–frequency domain using an appropriate segmentation. Each time series segment is defined based on a time and frequency pair to estimate a localized spectral peak in the spectrogram. At lower frequencies, the segment size is larger while the segment size reduces at higher frequencies, allowing a better estimation of long- and short-duration seasonal components, respectively. One of the main advantages of LSWA over LSSA is that LSWA can rigorously estimate the spectral components of a time series that exhibit non-stationary behavior, e.g., when amplitudes and frequencies of seasonal components change over time or there are short-duration signatures [9,12]. The LSWA has been widely applied to many applications, and its code is freely available in both MATLAB and python, namely, the least-squares wavelet software (LSWAVE) [13] and jumps upon spectrum and trend (JUST) [14].

In LSWAVE and JUST, depending on the specific goal and application, there are two options for selecting segment sizes: (1) frequency-dependent that is the focus of the present study, and (2) frequency-independent that is like the concept of the short-time Fourier transform (STFT) [3,10]. In the first option, the segment size depends on the time and frequency, i.e., as the frequency increases, the segment size

---

decreases and vice versa, allowing a more accurate estimation of short-duration signals with high frequency and long-duration signals with low frequency like in CWT [3,11]. In the second option, the segment size does not change across the frequency domain like in STFT, not suitable for analyzing time series that contain non-periodic and fast transient features [3,9]. Note that the mathematical derivations of the spectrograms and their stochastic confidence level surfaces are similar in both options.

One of the aims of LSSA/LSWA is to reduce or eliminate bias and increase efficiency (accuracy) in the estimation of the unknown parameters by considering the presence of (1) outliers, (2) heteroskedasticity (second order non-stationarity), and (3) possible incorrect model specification [10]. In LSSA/LSWA, simple basis functions are used to simultaneously and efficiently estimate trends of various forms and/or offsets (jumps), thus eliminating the first order non-stationarity. In LSSA/LSWA, the elimination or reduction of the effects of outliers and heteroscedasticity are achieved by appropriately formulating the covariance matrix of the time series (diagonal or fully populated) using various methods, such as variance component estimation, autocorrelation analysis, or the result of an estimation process [6,10]. In addition, the ability of LSSA/LSWA to suppress known systematic constituents of known form (trends, etc.) allows for the calculation of the post-fit residuals and their covariance matrix, used to test for residual outliers. Flagging those observations with lower weight and re-estimating the parameters can significantly mitigate the influence of outliers. Therefore, the results of this research respect the main principles of robust statistics and are robust and efficient.

Inspired by Fourier transform, several other time–frequency methods have been proposed in literature and are widely used in signal processing, such as Wigner-Ville transform [15,16], Gabor transform [17, 18], and Stockwell or S transform [19,20]. However, these methods are proposed for continuous signals or equally spaced time series, and they do not consider observational uncertainties nor constituents of known forms [9]. Foster proposed the weighted wavelet z-transform (WWZ) using the least-squares principle for analyzing unequally sampled time series and applied it to astronomical time series [21]. The WWZ is like CWT which obtains a spectrogram using a segmentation strategy. The WWZ was compared with LSWA in [10], where it was shown that LSWA is more rigorous for searching hidden signatures in time series while also accounting for measurement errors. In other words, unlike CWT and WWZ, LSWA allows users to search for low-amplitude periodic/aperiodic signals after suppressing or removing statistically significant peaks that are usually more dominant at low frequencies in many geoscience applications. The LSWA also considers observational uncertainties and their correlations in form of a covariance matrix. In both WWZ and LSWA, there is an option to consider a Gaussian weight function which assigns certain weights to each measurement of a segment. In fact, the measurements toward both ends of the segment receive relatively lower weights than those toward the center during the estimation of spectral peaks. The weighted L2 norm minimization technique in the weighted LSWA prevents spectral leakages in the spectrogram and produces an optimal time–frequency resolution, though it widens the frequency bandwidth of spectral peaks, e.g., see [10, Fig. 5c,d] and [12, Fig. 2.3].

The real-world application of the present research focuses on analyzing Global Navigation Satellite Systems (GNSS) position time series [22,23]. The GNSS refers to the international multi-constellation satellite systems, including GPS (United States), GLONASS (Russia), Galileo (European Union), and BeiDou (China), providing position, navigation, and timing services regionally or globally. The GNSS provides signals from space that transmit positioning and timing data to receivers. The receiver then utilizes the data to estimate its position with respect to a reference frame, such as the International Terrestrial Reference Frame (ITRF-2014) [24]. Thanks to an increased number of geodetic satellites, the accuracy of the GNSS position has been recently

improved to sub-centimeter and even millimeter levels [25]. The horizontal GNSS position time series, i.e., north and east directions, have been utilized for various purposes, including studying plate tectonic motion and earthquake activities, while the vertical component has been used for studying groundwater variation, ocean and atmospheric loading, and ice-snow loading among others [23,26].

The GNSS time series usually have jumps or discontinuities due to several reasons, such as earthquakes, antenna problems, replacement/maintenance of the station equipment, and change of the reference system, the location of which can be automatically determined by seasonal-trend and machine learning algorithms [14,25]. Many studies have focused on modeling noise in GNSS measurements. Kaczmarek and Kontny [27] modeled GNSS coordinate time series by the least-squares estimation and CWT to investigate the impact of measurement noise on signal estimation. Ji et al. [28] estimated signals from GNSS position time series by the weighted wavelet analysis. In another study, they proposed an extended singular spectrum analysis to directly analyze unequally spaced GNSS height time series [29]. The source of noise in GNSS measurements can be due to several factors, such as sensor error, atmospheric, and ground noise. Although GNSS processing agencies usually provide measurement errors and not the full covariance matrices, many researchers showed the presence of correlated noise in GNSS time series [30–32]. Considering the correlated noise may significantly bias the estimation of spectral peaks in the least-squares wavelet spectrogram (LSWS) [10,13]. Thus, it is crucial to understand and carefully consider random and systematic noises coming from the instrument/sensor itself prior to investigating the mechanism of geophysical process [33].

The main contributions of this research are summarized below.

- Presenting the mathematical derivation of the stochastic confidence level surface for LSWS, an unpublished part of the first author's PhD dissertation [12].
- Demonstrating the effect of measurement errors and missing data on signal estimation using LSWA via simulation.
- Analyzing GNSS time series for a station in Rome by LSWA and commenting on the spectral peaks in LSWS, considering jumps and measurement errors.
- Discussing potential causes of trends and seasonal components by analyzing GNSS time series provided by different agencies for the same station as well as analyzing an Interferometric Synthetic Aperture Radar (InSAR) time series that spatially includes the station position.

The rest of the manuscript is organized as follows. First, the theoretical parts of obtaining LSWS along with a computational optimization technique for it are reviewed in Sections 2.1 and 2.2. The mathematical derivation of the stochastic confidence level surface for LSWS is presented in Section 2.3. Then more description on how the LSWA weighting process works in LSWAVE and JUST in the cases of equally or unequally spaced time stamps is provided in Section 2.4. A simulation experiment is carried out in Section 3 to show the effects of noise and missing data on the spectrograms. A comprehensive analysis of the historical north, east, and up (NEU) position time series acquired at the GNSS receiver of Sapienza University of Rome is presented in Section 4 which also includes the trend estimation results for these time series before and after jump correction. Trend and spectrogram of an InSAR time series for period 2018–2022, representing the vertical displacement of a one-hectare area which contains the location of the GNSS receiver, are also estimated and compared with the ones for the GNSS height time series. Comments on potential impacts of jumps and known/unknown a-priori variance factor on LSWS and trend estimations as well as noises and missing data are provided in Section 5. This section also shows the analyses of GNSS height time series provided by other agencies for the same station, highlighting the uncertainties involved in the processing of GNSS time series for the same station by different providers. Finally, the conclusions are drawn in Section 6.

2. Least-squares wavelet analysis revisited

Suppose that $\mathbf{f} = [f(t_1), \ldots, f(t_n)]$ is a time series of size n, where t_j is the time when measurement $f(t_j)$ is acquired. Note that t_j can be unequally spaced, i.e., $t_j - t_{j-1}$ may not be the same for all j in $\{2, 3, \ldots, n\}$. The measurements in real-world applications have uncertainties, so assume that $\mathbf{C_f}$ is the covariance matrix associated with time series $\mathbf{f}$. Mathematically, vector $\mathbf{f}$ is in a Hilbert space metricized by $\mathbf{C_f}$ [6]. In many applications, only the standard deviations of the measurements are provided, i.e., $f(t_i)$ is either statistically independent from $f(t_j)$ or their dependency is neglected, so the covariance matrix is diagonal. Let $\mathbf{P} = \mathbf{C_f}^{-1}$ be the weight matrix associated with $\mathbf{f}$. Now let $\mathbf{y}$ be a time series segment of size R ($R \leq n$), determined for a time–frequency pair, and $\mathbf{P_y}$ be the principal submatrix of $\mathbf{P}$ associated with $\mathbf{y}$ [10].

2.1. The normalized least-squares wavelet spectrogram (LSWS)

In practice, there might be certain components that are physically known and considered systematic noise, such as trends (linear or non-linear), e.g., due to displacement, so they can be estimated and removed. Thus, consider $\mathbf{y}$ containing q constituents of known forms, $\mathbf{\Phi}_1, \mathbf{\Phi}_2, \ldots, \mathbf{\Phi}_q$, e.g., trends or sinusoids of constant frequencies where their coefficients are not known. For example, $\mathbf{\Phi}_1$ is the column vector of all ones with dimension R, and $\mathbf{\Phi}_2$ is the time column vector of the segment. Note that the coefficients of $\mathbf{\Phi}_1$ and $\mathbf{\Phi}_2$, estimated after the LSWA process, represent the intercept and slope of the linear trend fitted to the segment, respectively. Now define the following design matrices

$$\mathbf{\Phi} = \left[\cos\left(2\pi\omega\, \mathbf{t_y}\right),\ \sin\left(2\pi\omega\, \mathbf{t_y}\right) \right] \tag{1}$$

$$\underline{\mathbf{\Phi}} = \left[\mathbf{\Phi}_1, \mathbf{\Phi}_2, \ldots, \mathbf{\Phi}_q \right], \tag{2}$$

$$\overline{\mathbf{\Phi}} = \left[\underline{\mathbf{\Phi}},\ \mathbf{\Phi} \right], \tag{3}$$

where ω is a given cyclic frequency and $\mathbf{t_y}$ is the time vector of segment $\mathbf{y}$. Note that the dimensions of $\mathbf{\Phi}$, $\underline{\mathbf{\Phi}}$, and $\overline{\mathbf{\Phi}}$ are $R \times 2$, $R \times q$, and $R \times (q+2)$, respectively.

The known constituents of each segment (systematic noise) do not have to be removed from the segment before estimation of the spectral peaks corresponding to the segment. However, it speeds up the computation if these constituents are estimated first and removed from the segment while their correlations with the rest of segment components are carried forward during the estimation of peak [2,10]. Thus, LSWA first estimates the coefficients of columns of $\underline{\mathbf{\Phi}}$ in Eq. (2), then it removes their contributions from segment $\mathbf{y}$ to obtain the residual segment $\hat{\mathbf{g}}$. More precisely, let $\mathbf{y} = \underline{\mathbf{\Phi}}\,\underline{\mathbf{c}}$ to estimate $\underline{\mathbf{c}}$ using the least-squares method as

$$\underline{\hat{\mathbf{c}}} = \underline{\mathbf{N}}^{-1} \underline{\mathbf{\Phi}}^{\mathrm{T}} \mathbf{P_y} \mathbf{y}, \tag{4}$$

where $\underline{\mathbf{N}} = \underline{\mathbf{\Phi}}^{\mathrm{T}} \mathbf{P_y} \underline{\mathbf{\Phi}}$, and so $\hat{\mathbf{g}} = \mathbf{y} - \underline{\mathbf{\Phi}}\,\underline{\hat{\mathbf{c}}}$. Then use the model $\mathbf{y} = \overline{\mathbf{\Phi}}\,\overline{\mathbf{c}} = \underline{\mathbf{\Phi}}\,\underline{\mathbf{c}} + \mathbf{\Phi}\,\mathbf{c}$ to estimate $\mathbf{c}$ as

$$\hat{\mathbf{c}} = \mathbf{N}^{-1} \mathbf{\Phi}^{\mathrm{T}} \mathbf{P_y} \hat{\mathbf{g}}, \tag{5}$$

where $\mathbf{N} = \mathbf{\Phi}^{\mathrm{T}} \mathbf{P_y} \mathbf{\Phi} - \mathbf{\Phi}^{\mathrm{T}} \mathbf{P_y} \underline{\mathbf{\Phi}}\, \underline{\mathbf{N}}^{-1} \underline{\mathbf{\Phi}}^{\mathrm{T}} \mathbf{P_y} \mathbf{\Phi}$ (see Section 2.2 for the derivation). Note that $\hat{\mathbf{c}}$ is a column vector of dimension two whose entries are the estimated coefficients of the cosine and sine function at frequency ω. The amplitude LSWS is defined as [14]:

$$s_{\mathrm{amp}} = \sqrt{\hat{\mathbf{c}}^{\mathrm{T}} \hat{\mathbf{c}}}. \tag{6}$$

Let $\mathbf{J} = \mathbf{\Phi} \mathbf{N}^{-1} \mathbf{\Phi}^{\mathrm{T}} \mathbf{P_y}$. The normalized LSWS (LSWS hereafter) is defined by the following equation:

$$s = \frac{\hat{\mathbf{g}}^{\mathrm{T}} \mathbf{P_y} \mathbf{\Phi}\, \hat{\mathbf{c}}}{\hat{\mathbf{g}}^{\mathrm{T}} \mathbf{P_y} \hat{\mathbf{g}}} = \frac{\hat{\mathbf{g}}^{\mathrm{T}} \mathbf{P_y} \mathbf{J} \hat{\mathbf{g}}}{\hat{\mathbf{g}}^{\mathrm{T}} \mathbf{P_y} \hat{\mathbf{g}}}, \tag{7}$$

Note that s is in $(0, 1)$, showing the amount of sine waveforms at cyclic frequency ω contained in the residual segment $\mathbf{y}$. The value of s, after multiplied by 100, is named the percentage variance.

Geometrically, $\mathbf{y}$ is first orthogonally projected onto the manifold generated by columns of $\underline{\mathbf{\Phi}}$. The residual segment $\hat{\mathbf{g}}$ is orthogonal to the manifold generated by columns of $\underline{\mathbf{\Phi}}$. Next, $\hat{\mathbf{g}}$ is orthogonally projected onto the manifold generated by the columns of $\overline{\mathbf{\Phi}}$, and the projected vector is then orthogonally projected back onto $\hat{\mathbf{g}}$ to obtain $\mathbf{\Phi}\,\hat{\mathbf{c}}$. Finally, the ratio of the weighted length of the projected vector $\mathbf{\Phi}\,\hat{\mathbf{c}}$ to the weighted length of $\hat{\mathbf{g}}$ shows the estimated spectral peak for the residual segment $\hat{\mathbf{g}}$ as given by Eq. (7).

2.2. Computational optimization of the least-squares wavelet analysis

A similar methodology is used as in [4,5] to obtain Eq. (5). From the model $\mathbf{y} = \overline{\mathbf{\Phi}}\,\overline{\mathbf{c}} = \underline{\mathbf{\Phi}}\,\underline{\mathbf{c}} + \mathbf{\Phi}\,\mathbf{c}$, coefficient vector $\overline{\mathbf{c}}$ is estimated by the least-squares method as $\hat{\overline{\mathbf{c}}} = \overline{\mathbf{N}}^{-1} \overline{\mathbf{\Phi}}^{\mathrm{T}} \mathbf{P_y} \mathbf{y}$, where $\overline{\mathbf{N}} = \overline{\mathbf{\Phi}}^{\mathrm{T}} \mathbf{P_y} \overline{\mathbf{\Phi}}$. Now $\overline{\mathbf{N}}^{-1}$ can be written as

$$\overline{\mathbf{N}}^{-1} = \left[\begin{array}{cc} \underline{\mathbf{\Phi}}^{\mathrm{T}} \mathbf{P_y} \underline{\mathbf{\Phi}} & \underline{\mathbf{\Phi}}^{\mathrm{T}} \mathbf{P_y} \mathbf{\Phi} \\ \mathbf{\Phi}^{\mathrm{T}} \mathbf{P_y} \underline{\mathbf{\Phi}} & \mathbf{\Phi}^{\mathrm{T}} \mathbf{P_y} \mathbf{\Phi} \end{array} \right]^{-1} = \left[\begin{array}{cc} \mathbf{M_1} & \mathbf{M_2} \\ \mathbf{M_3} & \mathbf{M_4} \end{array} \right], \tag{8}$$

where

$$\mathbf{M_1} = \left(\underline{\mathbf{\Phi}}^{\mathrm{T}} \mathbf{P_y} \underline{\mathbf{\Phi}} - \underline{\mathbf{\Phi}}^{\mathrm{T}} \mathbf{P_y} \mathbf{\Phi}\, (\mathbf{\Phi}^{\mathrm{T}} \mathbf{P_y} \mathbf{\Phi})^{-1} \mathbf{\Phi}^{\mathrm{T}} \mathbf{P_y} \underline{\mathbf{\Phi}} \right)^{-1}$$
$$= \underline{\mathbf{N}}^{-1} + \underline{\mathbf{N}}^{-1} \underline{\mathbf{\Phi}}^{\mathrm{T}} \mathbf{P_y} \mathbf{\Phi}\, \mathbf{M_4}\, \mathbf{\Phi}^{\mathrm{T}} \mathbf{P_y} \underline{\mathbf{\Phi}}\, \underline{\mathbf{N}}^{-1}, \tag{9}$$

$$\mathbf{M_2} = -\mathbf{M_1}\, \underline{\mathbf{\Phi}}^{\mathrm{T}} \mathbf{P_y} \mathbf{\Phi}\, (\mathbf{\Phi}^{\mathrm{T}} \mathbf{P_y} \mathbf{\Phi})^{-1} = -\underline{\mathbf{N}}^{-1}\, \underline{\mathbf{\Phi}}^{\mathrm{T}} \mathbf{P_y} \mathbf{\Phi}\, \mathbf{M_4}, \tag{10}$$

$$\mathbf{M_3} = -\mathbf{M_4}\, \mathbf{\Phi}^{\mathrm{T}} \mathbf{P_y} \underline{\mathbf{\Phi}}\, \underline{\mathbf{N}}^{-1}, \tag{11}$$

$$\mathbf{M_4} = \left(\mathbf{\Phi}^{\mathrm{T}} \mathbf{P_y} \mathbf{\Phi} - \mathbf{\Phi}^{\mathrm{T}} \mathbf{P_y} \underline{\mathbf{\Phi}}\, \underline{\mathbf{N}}^{-1} \underline{\mathbf{\Phi}}^{\mathrm{T}} \mathbf{P_y} \mathbf{\Phi} \right)^{-1}, \tag{12}$$

and $\underline{\mathbf{N}} = \underline{\mathbf{\Phi}}^{\mathrm{T}} \mathbf{P_y} \underline{\mathbf{\Phi}}$. It is assumed that matrices $\mathbf{\Phi}^{\mathrm{T}} \mathbf{P_y} \mathbf{\Phi}$ and $\underline{\mathbf{N}}$ are regular. Note that the number of rows in $\underline{\mathbf{\Phi}}$ and $\mathbf{\Phi}$ is equal to the window size in LSWA. Matrix $\underline{\mathbf{N}}$ is regular when the columns of $\underline{\mathbf{\Phi}}$, consisting of the constituents of known forms, are linearly independent. Depending on the constituents of known forms and irregularity in time sampling, the window size should be large enough (> the number of constituents of known forms), so that the column vectors are mutually independent and $\underline{\mathbf{N}}$ is regular, or else a pseudo-inverse may be computed [34].

$$\left[\begin{array}{c} \mathbf{x} \\ \hat{\mathbf{c}} \end{array} \right] = \hat{\overline{\mathbf{c}}} = \overline{\mathbf{N}}^{-1} \overline{\mathbf{\Phi}}^{\mathrm{T}} \mathbf{P_y} \mathbf{y} = \left[\begin{array}{cc} \mathbf{M_1} & \mathbf{M_2} \\ \mathbf{M_3} & \mathbf{M_4} \end{array} \right] \left[\begin{array}{c} \underline{\mathbf{\Phi}}^{\mathrm{T}} \mathbf{P_y} \mathbf{y} \\ \mathbf{\Phi}^{\mathrm{T}} \mathbf{P_y} \mathbf{y} \end{array} \right], \tag{13}$$

the following equation can be derived:

$$\hat{\mathbf{c}} = \mathbf{M_3}\, \underline{\mathbf{\Phi}}^{\mathrm{T}} \mathbf{P_y} \mathbf{y} + \mathbf{M_4}\, \mathbf{\Phi}^{\mathrm{T}} \mathbf{P_y} \mathbf{y}$$
$$= -\mathbf{M_4}\, \mathbf{\Phi}^{\mathrm{T}} \mathbf{P_y} \underline{\mathbf{\Phi}}\, \underline{\mathbf{N}}^{-1} \underline{\mathbf{\Phi}}^{\mathrm{T}} \mathbf{P_y} \mathbf{y} + \mathbf{M_4}\, \mathbf{\Phi}^{\mathrm{T}} \mathbf{P_y} \mathbf{y}$$
$$= \mathbf{M_4}\, \mathbf{\Phi}^{\mathrm{T}} \mathbf{P_y} \left(\mathbf{y} - \underline{\mathbf{\Phi}}\, \underline{\mathbf{N}}^{-1} \underline{\mathbf{\Phi}}^{\mathrm{T}} \mathbf{P_y} \mathbf{y} \right)$$
$$= \mathbf{N}^{-1} \mathbf{\Phi}^{\mathrm{T}} \mathbf{P_y} \hat{\mathbf{g}}, \tag{14}$$

where $\mathbf{N} = \mathbf{M_4}^{-1} = \mathbf{\Phi}^{\mathrm{T}} \mathbf{P_y} \mathbf{\Phi} - \mathbf{\Phi}^{\mathrm{T}} \mathbf{P_y} \underline{\mathbf{\Phi}}\, \underline{\mathbf{N}}^{-1} \underline{\mathbf{\Phi}}^{\mathrm{T}} \mathbf{P_y} \mathbf{\Phi}$, and $\hat{\mathbf{g}} = \mathbf{y} - \underline{\mathbf{\Phi}}\, \underline{\mathbf{N}}^{-1} \underline{\mathbf{\Phi}}^{\mathrm{T}} \mathbf{P_y} \mathbf{y}$ is the estimated residual segment. Note that for each frequency, $\mathbf{N}$ is a square matrix of order two, and so its inverse is computationally efficient.

2.3. Stochastic significance of peaks in LSWS

One of the advantages of LSWS is that the significance of the peaks can be statistically tested at a certain confidence level in a rigorous manner. For theoretical derivation of the statistical tests in LSWS, an assumption is made that the observed time series is derived from a population of random variables following a multi-dimensional normal distribution. Foremost, note that the normality assumption of observations has nothing to do with the calculation of spectrogram. Making this assumption, it is possible to verify which peak is statistically significant in the spectrogram, so it can be suppressed/removed from the

spectrogram to search other hidden signatures, e.g., weaker periodic or aperiodic components [6,10]. The process of suppressing/removing spectral peaks is simply done by appending horizontally the column vectors of cosine and sine at the known frequency to $\underline{\boldsymbol{\Phi}}$ in Eq. (2). Note that unlike LSS, the stochastic significance of peaks in LSWS, given by Eq. (7), depends on frequency [10]. Following a similar technique described in [5,6,35], it is shown below how the probability distribution function of LSWS is derived with a known covariance matrix.

The covariance matrix is always Hermitian, i.e., it is equal to its conjugate transpose, and positive semi-definite. For simplicity, it is assumed that covariance matrix $\mathbf{C_f}$ associated with $\mathbf{f}$ is positive definite and so regular. Thus, $\mathbf{P} = \mathbf{C_f}^{-1}$ is positive definite, and so are all its principal submatrices $\mathbf{P_y}$ [36]. Note that in case of singular $\mathbf{C_f}$, one may obtain the pseudo-inverse of $\mathbf{C_f}$ and obtain similar results [6,34]. A square matrix $\mathbf{M}$ is called idempotent if $\mathbf{MM} = \mathbf{M}$. Idempotent matrices have many desirable properties. For instance, $\text{rank}(\mathbf{M}) = \text{trace}(\mathbf{M})$ [36].

Let $\overline{\mathbf{J}} = \overline{\boldsymbol{\Phi}}\,\overline{\mathbf{N}}^{-1}\overline{\boldsymbol{\Phi}}^{\mathrm{T}}\mathbf{P_y}$, $\underline{\mathbf{J}} = \underline{\boldsymbol{\Phi}}\,\underline{\mathbf{N}}^{-1}\underline{\boldsymbol{\Phi}}^{\mathrm{T}}\mathbf{P_y}$ and $\mathbf{J} = \boldsymbol{\Phi}\mathbf{N}^{-1}\boldsymbol{\Phi}^{\mathrm{T}}\mathbf{P_y}$, where $\overline{\mathbf{N}} = \overline{\boldsymbol{\Phi}}^{\mathrm{T}}\mathbf{P_y}\overline{\boldsymbol{\Phi}}$, $\underline{\mathbf{N}} = \underline{\boldsymbol{\Phi}}^{\mathrm{T}}\mathbf{P_y}\underline{\boldsymbol{\Phi}}$ and $\mathbf{N} = \boldsymbol{\Phi}^{\mathrm{T}}\mathbf{P_y}\boldsymbol{\Phi} - \boldsymbol{\Phi}^{\mathrm{T}}\mathbf{P_y}\underline{\mathbf{J}}\boldsymbol{\Phi}$. It is straightforward to verify that $\overline{\mathbf{J}}$ and $\underline{\mathbf{J}}$ are idempotent. As shown in Appendix, Eq. (7) is identical to

$$s = \frac{\mathbf{y}^{\mathrm{T}}\mathbf{P_y}(\overline{\mathbf{J}} - \underline{\mathbf{J}})\,\mathbf{y}}{\mathbf{y}^{\mathrm{T}}\mathbf{P_y}(\mathbf{I} - \underline{\mathbf{J}})\,\mathbf{y}}. \tag{15}$$

The denominator of Eq. (15) can be written as $\mathbf{y}^{\mathrm{T}}\mathbf{P_y}(\mathbf{I} - \underline{\mathbf{J}})\,\mathbf{y} = \mathbf{y}^{\mathrm{T}}\mathbf{P_y}(\overline{\mathbf{J}} - \underline{\mathbf{J}})\,\mathbf{y} + \mathbf{y}^{\mathrm{T}}\mathbf{P_y}(\mathbf{I} - \overline{\mathbf{J}})\,\mathbf{y}$. Let $Q_s = \mathbf{y}^{\mathrm{T}}\mathbf{P_y}(\overline{\mathbf{J}} - \underline{\mathbf{J}})\,\mathbf{y}$ (signal) and $Q_n = \mathbf{y}^{\mathrm{T}}\mathbf{P_y}(\mathbf{I} - \overline{\mathbf{J}})\,\mathbf{y}$ (noise). Eq. (15) can be written as

$$s = \frac{Q_s}{Q_s + Q_n} = \left(1 + \frac{Q_n}{Q_s}\right)^{-1}. \tag{16}$$

Noting that $\overline{\mathbf{J}} - \underline{\mathbf{J}}$ is idempotent and

$$\begin{aligned}
\text{rank}\left(\mathbf{P_y}(\overline{\mathbf{J}} - \underline{\mathbf{J}})\right) &= \text{rank}(\overline{\mathbf{J}} - \underline{\mathbf{J}}) \\
&= \text{trace}(\overline{\mathbf{J}} - \underline{\mathbf{J}}) \\
&= \text{trace}(\overline{\mathbf{J}}) - \text{trace}(\underline{\mathbf{J}}) \\
&= q + 2 - q = 2, \tag{17}
\end{aligned}$$

random variable Q_s is distributed as chi-square distribution with 2 degrees of freedom, i.e., $Q_s \sim \chi_2^2$, where symbol $\sim$ is used to show that a random variable *follows* a distribution [37, Chapter 9.8]. Similarly, noting that $\mathbf{I} - \overline{\mathbf{J}}$ is idempotent and

$$\begin{aligned}
\text{rank}\left(\mathbf{P_y}(\mathbf{I} - \overline{\mathbf{J}})\right) &= \text{rank}(\mathbf{I} - \overline{\mathbf{J}}) \\
&= \text{trace}(\mathbf{I} - \overline{\mathbf{J}}) \\
&= \text{trace}(\mathbf{I}) - \text{trace}(\overline{\mathbf{J}}) \\
&= R - (q + 2) = \Re, \tag{18}
\end{aligned}$$

random variable Q_n is distributed as chi-square distribution with $\Re$ degrees of freedom, i.e., $Q_n \sim \chi_{\Re}^2$ [37, Chapter 9.8]. Since $\mathbf{P_y}(\mathbf{I} - \overline{\mathbf{J}})\mathbf{P_y}^{-1}\mathbf{P_y}(\overline{\mathbf{J}} - \underline{\mathbf{J}}) = \mathbf{P_y}(\overline{\mathbf{J}} - \underline{\mathbf{J}} - \overline{\mathbf{J}} + \underline{\mathbf{J}}) = \mathbf{0}$, random variables Q_s and Q_n are statistically independent, and so Q_n/Q_s follows $(\Re/2)F_{\Re,2}$, where F is the F-distribution [37, Chapter 9.8]. Therefore, LSWS given by Eq. (7) or (30) or (16) (all identical) follows the beta distribution with parameters 1 and $\Re/2$, i.e., $s \sim \beta_{1,\Re/2}$.

The null hypothesis H_0 and alternative hypothesis H_1 are defined as follows:

$$H_0 : \quad \frac{Q_n}{Q_s} \geq \frac{\Re}{2} F_{\Re,2,\alpha}, \tag{19}$$

$$H_1 : \quad \frac{Q_n}{Q_s} < \frac{\Re}{2} F_{\Re,2,\alpha}, \tag{20}$$

where α is the significance level (usually $\alpha = 0.01$ or $\alpha = 0.05$). Based on the null hypothesis, one may only consider the lower tail end of F because large values of ratio Q_n/Q_s mean that the noise is significantly

larger than the signal, and so the signal is undetectable [6]. The stochastic surface at $(1 - \alpha)$ confidence level for the spectrogram given by Eq. (16) is

$$\zeta = \left(1 + \frac{\Re}{2} F_{\Re,2,\alpha}\right)^{-1}. \tag{21}$$

If $s > \zeta$, then H_0 is rejected, and spectral peak s is statistically significant at $(1 - \alpha)$ confidence level. Note that the critical value given by Eq. (21) depends on the segment size which may vary for each time–frequency pair.

Using the relation $F_{\Re,2,\alpha} = F_{2,\Re,1-\alpha}^{-1} = (2/\Re)(\alpha^{-2/\Re} - 1)^{-1}$ [5,6,34], Eq. (21) can be written as

$$\zeta = \left(1 + \frac{1}{\alpha^{-2/\Re} - 1}\right)^{-1} = 1 - \alpha^{2/\Re}. \tag{22}$$

It is worthwhile mentioning that LSS of a time series with known covariance matrix follows the beta distribution with parameter values 1 and $(n - q - 2)/2$, and so the critical value at $(1 - \alpha)$ confidence level for LSS is $\zeta = 1 - \alpha^{2/(n-q-2)}$ [6]. In other words, in equations above assume that $R = n$, where n is the size of time series $\mathbf{f}$, and $\mathbf{P_y} = \mathbf{P}$. This critical value is frequency-independent for LSS but is frequency-dependent for LSWS [10]. Therefore, the larger the segment size, in the case of low frequency peaks in a spectrogram, the more significant the smaller peaks are in the spectrogram from the statistical point of view, and vice versa. In other words, at a fixed confidence level, the peaks at higher frequencies should be stronger, i.e., should have higher percentage variance, to be statistically significant at that confidence level. The spectral peaks in LSWS generally must be stronger to be statistically significant when there are missing measurements within a given window because the degrees of freedom, defining the stochastic confidence level surface in Eq. (22), is smaller than when there are no missing measurements within the same window.

2.4. Empirical and statistical weights in LSWA

To better understand how LSWA estimates the spectral peaks when using a Gaussian weight function, an example is illustrated in Fig. 1(a). In this example, the sine waveforms have six complete cycles which construct a Morlet wavelet [38] when they are multiplied by the Gaussian weights. The cycles toward both ends of the Morlet wavelet attenuate to zero, and the six cycles along with Morlet coefficient 0.0125 are the default settings of LSWA in LSWAVE and JUST as recommended in [9,11,21]. Note that in LSWA, the Gaussian weights adapt the sinusoids to Morlet wavelet in the least-squares sense. In Fig. 1(b), the center of the Morlet wavelet is at the window center shown in brown. The process of fitting the sine waveforms to the segment considering the Gaussian weights is done within the window at a given frequency to estimate the corresponding spectral peak. In the earlier version of LSWA available in LSWAVE, the window translates over time stamps of a time series, so no spectral peaks are estimated at periods where there are no available measurements [10,13]. However, the new version of LSWA available in JUST has a new feature that the user can select a set of equally spaced times between the time domain of the provided time series to estimate an equally spaced time spectrogram [14]. For example, for a daily GNSS time series with many missing values, a spectrogram can be estimated for a set of daily spaced times. In another example, a spectrogram can be estimated for a set of hourly spaced values for an astronomical time series with inherently unequally spaced times.

To see how this process is done, in Fig. 1(b), an equally spaced time sequence is displayed by red squares for computing a spectrogram. In this case, the window center (Gaussian center) is located at the red square, highlighted by the vertical arrow, and the window translates from one red square to another while a spectral peak will be estimated by Eq. (7) at each step. In the LSWA tool in JUST, when the user decides to decompose a time series into an equally spaced time domain,
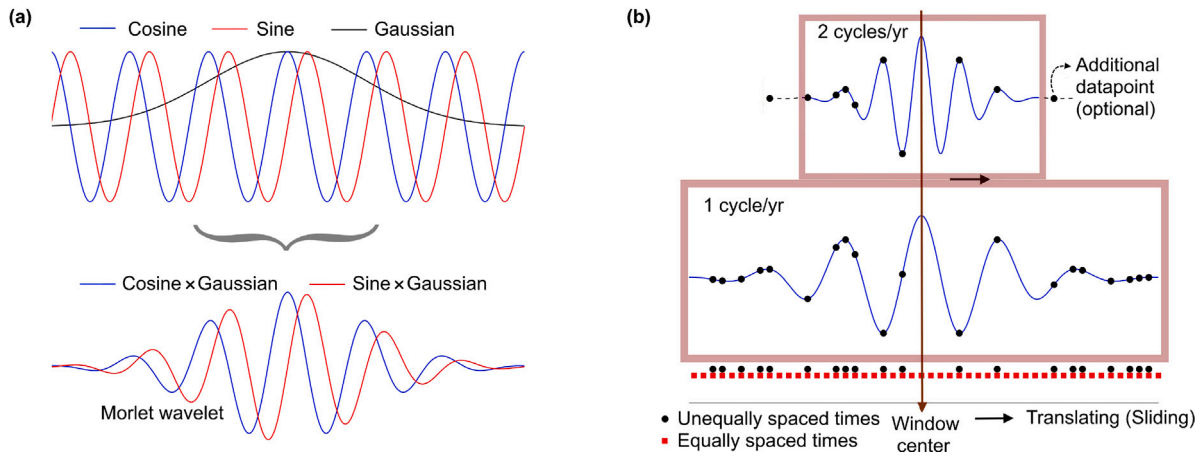
Fig. 1. (a) a Morlet wavelet derived by multiplication of Gaussian and sinusoidal functions, and (b) a case of unequally spaced time stamps in black circles and equally spaced time stamps in red squares for estimating spectral peaks on the equally spaced time stamps. Only the real part of the Morlet wavelet is shown in panel (b) for brevity.

the segmentation or windowing will be done on the selected equally spaced time sequence for each frequency [10]. However, there is a possibility that the windows at higher frequencies do not include the minimum required number of measurements for spectral peak estimation. For example, in Fig. 1(b), there are 20 points (black circles) at 1 cycle/year inside the window shown by the brown square while there are 8 points within the window at 2 cycles/year shown by the brown window. Since the wavelength is inversely proportional to frequency, the window length (time difference between both sides of the window) at 2 cycles/year is half of the window length at 1 cycle/year; however, since there are missing data, the smaller window contains 8 points (window size 8) instead of 10 points (window size 10). This could result in the singularity of $\mathbf{N}$ in Eq. (5) at higher frequencies when there are many missing values [10]. Using additional points from each side of the window to enlarge its size is a good solution; however, when the time series are strongly non-stationary, it is recommended to assign relatively lower weights to the measurements toward both ends of the window which can be done by the Gaussian weights. Therefore, it is recommended that users enlarge the window size at higher frequencies by selecting larger values for window parameters, i.e., by increasing L_1, the number of sinusoidal cycles, and/or L_0, the number of additional datapoints [10,14]. Note that enlarging the window to include more measurements will reduce the critical percentage variance. Finally, if the measurement errors are also provided, their squared inverses may be multiplied by the Gaussian weights within each window before estimating a spectrogram [13,14].

Note that the choice of the weight matrix $\mathbf{P_y}$ assigned to segment $\mathbf{y}$ depends on the application and purpose. This matrix may be diagonal or partially or fully populated. The weight matrix should be positive definite to satisfy the weighted L2 norm minimization criterion in LSWA. This matrix may also be ignored in LSWA, i.e., case of ordinary LSWA [10]. When this matrix is diagonal, it is treated as a vector for the sake of computational efficiency [13].

3. A simulation experiment

To investigate how the presence of noises, such as flicker and white as well as the amount of missing values may contaminate spectrograms, a 7-year-long daily displacement time series is simulated as follows:

$$f(t) = f_1(t) + f_2(t) + f_3(t) + f_4(t) \tag{23}$$

where $f_1(t)$ is a flicker noise (inverse frequency) generated by MATLAB commands "firls", "rand", and "filtfilt". First, the command "firls" is used to return an array containing 43 coefficients of an order-42 finite impulse response (FIR) filter with an equally spaced set of frequencies from 0 to 1 (fv) and amplitude response of $1/(1 + fv^2)$.

Then "rand" is used to generate 2555 random numbers between 0 and 1 which together with the output of "firls" are entered in "filtfilt" to produce $f_1(t)$ of size 2555, corresponding to 7 years of daily samples, see Fig. 2(a). The second component $f_2(t)$ is a Gaussian white noise generated by MATLAB command "randn", see Fig. 2(b). Also, $f_3(t) = (0.3+0.1t)\sin(2\pi t)$ and $f_4(t) = -0.2t$, where $t = [1, 2, 3, \ldots, 2555]/365.256$, see Fig. 2.

3.1. Amplitude and normalized LSWSs

Fig. 3 shows the amplitude and normalized LSWSs of the simulated time series and its components. The amplitude LSWSs are estimated using Eq. (6). It is crucial to understand how to interpret the spectral peaks in the amplitude and normalized LSWSs. Fig. 3(c) shows the amplitude of annual peaks is increasing over time as can be seen in Fig. 2(c) while Fig. 3(d) shows the percentage variance of 100% for the annual peaks over time as expected. The flicker noise presents some low frequency peaks (annual and semi-annual) mainly during 2015–2016 and with a lower amplitude during 2016–2018, see Fig. 3(a). These peaks have contaminated the spectrograms and have a significant impact on estimating the annual peaks, i.e., the signal in Fig. 2(c) that may represent ground deformation (see also the next section). Comparing Fig. 3(b) and (h), the accuracy of LSWA in simultaneous estimating and removing the annual peaks can be observed.

3.2. Effect of missing values on spectrogram

To show how effectively LSWA can estimate the signals in presence of noises and missing values, the same simulated time series shown in Fig. 2(e) is employed. Different percentage amount of data (20%, 40%, 60%, 80%) are removed from the time series at random, and an amplitude LSWS is estimated for each case, see Fig. 4. The estimated annual signal obtained from each amplitude LSWS (ordinary) along with its root mean square error (RMSE) is shown in Fig. 4(b). The time interval for all the amplitude LSWSs is daily, and the annual signal is obtained from each of these LSWSs. The RMSE of the annual signal without simultaneous fitting of a linear trend within each window is also calculated as 0.065 mm, showing a larger error as compared to the case when a linear trend is also fitted simultaneously within each window (RMSE = 0.059 mm). Most of the error in estimating the annual signal is observed during 2015–2017, mainly due to the presence of flicker noise as mentioned in the previous subsection. Considering appropriate weights, $\mathbf{P_y}$, defined from the simulated flicker noise, has improved the annual signal estimation, see Table 1. This table also shows that the RMSE of the weighted LSWA when estimating the annual signal is approximately 0.02 mm less than the ordinary
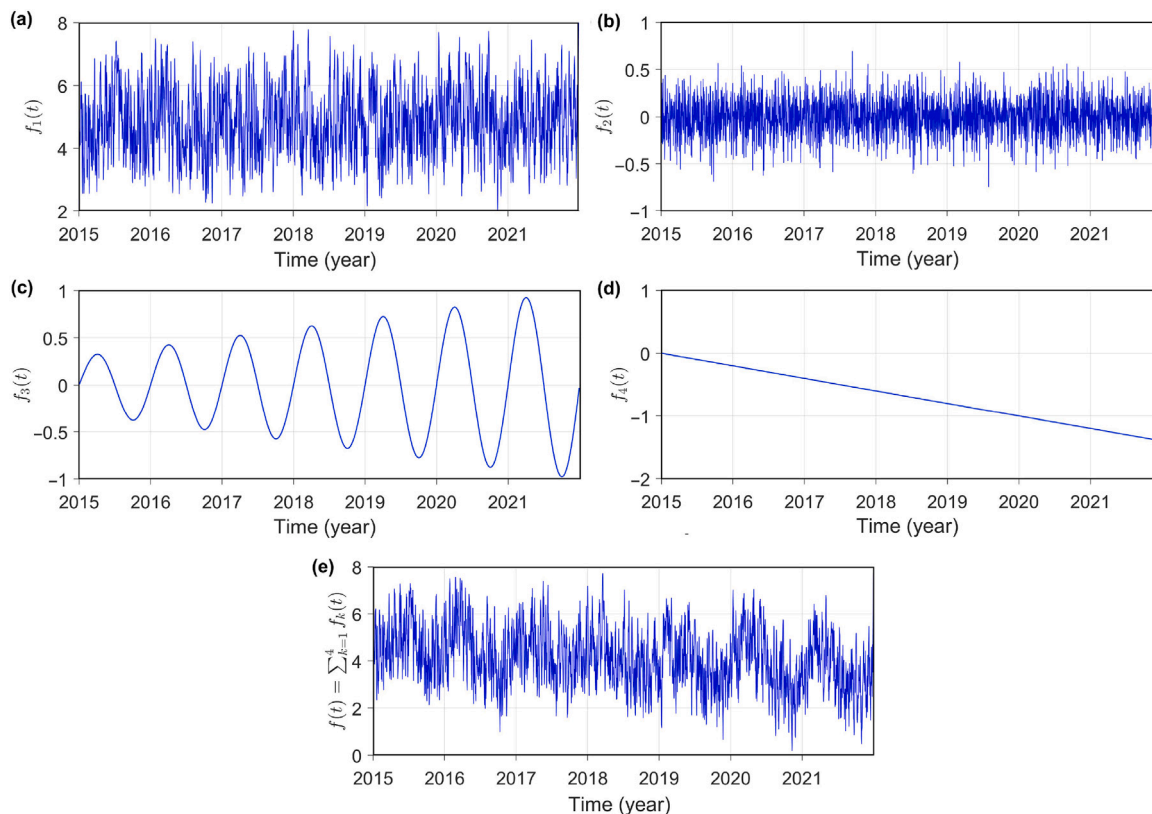
Fig. 2. The components of a 7-year-long daily simulated time series: (a) $f_1(t)$ is a flicker noise, (b) $f_2(t)$ is a Gaussian white noise, (c) $f_3(t)$ is an annual component whose amplitude increases over time, (d) $f_4(t)$ is a linear trend, and (e) $f(t)$ is the simulated time series.

Table 1
RMSE comparison between the ordinary and weighted LSWA for estimating the annual signal (ground truth) shown in Fig. 2(c).

Amount of missing data	0%	20%	40%	60%	80%
RMSE (Ordinary LSWA)	0.059	0.071	0.083	0.092	0.125
RMSE (Weighted LSWA)	0.047	0.054	0.061	0.064	0.087

LSWA. It is worth noting that in many monitoring techniques, such as InSAR and very long baseline interferometry (VLBI), time series may have many missing values due to atmospheric conditions and sensor issues, highlighting the importance of signal processing tools, such as LSWA (e.g., [39,40]). In this work, also note that regardless of whether the input time series is equally spaced or not, all the spectrograms are estimated on regular daily time intervals (equally spaced). The cyclic frequencies are also equally spaced, incrementing by 0.1 cycles/year.

4. A real-world application

In this section, LSWA is applied to analyze geodetic time series that are unequally spaced and contain jumps. First the seasonal and trend components for the entire time series are estimated by LSWAVE. Next, the stochastic surfaces for spectrograms in two cases of equally spaced and unequally spaced time domains are demonstrated. Finally, some comments on the stochastic significance of spectral peaks in the spectrograms are presented.

4.1. Study site and datasets

The GNSS receiver with station ID (M0SE00ITA) is in the Faculty of Civil and Industrial Engineering at Sapienza University of Rome,

near the Saint Peter in Chains church close to the Colosseum, Fig. 5. The north, east, and up position time series shown in red circles in Fig. 6(a)–(c), respectively, are downloaded from https://doi.org/10.13120/b6aj-2s32 (Last accessed on 24/09/2023) [41]. The north-east-up (NEU) reference position is 41.89311°N, 12.49326°E, and 120.567 m above the mean sea level (IGb14/WGS84). Each time series shows the difference between the measured and NEU reference positions and centralized using its mean [41]. The NEU time series have four known discontinuities or jumps whose dates are provided by the Royal Observatory of Belgium website http://www.epncb.oma.be/ (Last accessed on 24/09/2023). The jump locations are shown by the brown dashed lines in Fig. 6. The cause of the most significant jumps on 19/06/2007 and 13/04/2012 was due to antenna changes while the other two jumps on 06/04/2009 and 30/10/2016 with relatively lower magnitudes were due to impact of L'Aquila earthquake occurred near L'Aquila, the capital of Abruzzo, and the Norcia earthquake occurred near Norcia in the province of Perugia in Umbria, respectively [42,43]. The NEU time series have a size of 6252 with 3.34% missing values. Fig. 7 shows the number of measurements for each year. Note that the start and end dates of the daily time series are 15/10/2004 and 30/06/2022, respectively.

InSAR is another advanced remote sensing technique for ground deformation monitoring [44,45]. The European Ground Motion Service (EGMS) has recently released a product for ground motion monitoring which utilizes InSAR data derived from Sentinel-1 satellites for both ascending and descending orbits https://egms.land.copernicus.eu/ (Last accessed on 01/01/2024). The EGMS Ortho 2018–2022 product contains regularly sampled spatial points (100 m grid), where each point is associated with a displacement time series with sampling rate of 6-day [46]. To further evaluate the trend results and spectral peaks in LSWS, an EGMS Ortho-Vertical time series is also employed, representing the ground vertical motion of a one hectare area which includes the GNSS receiver location.
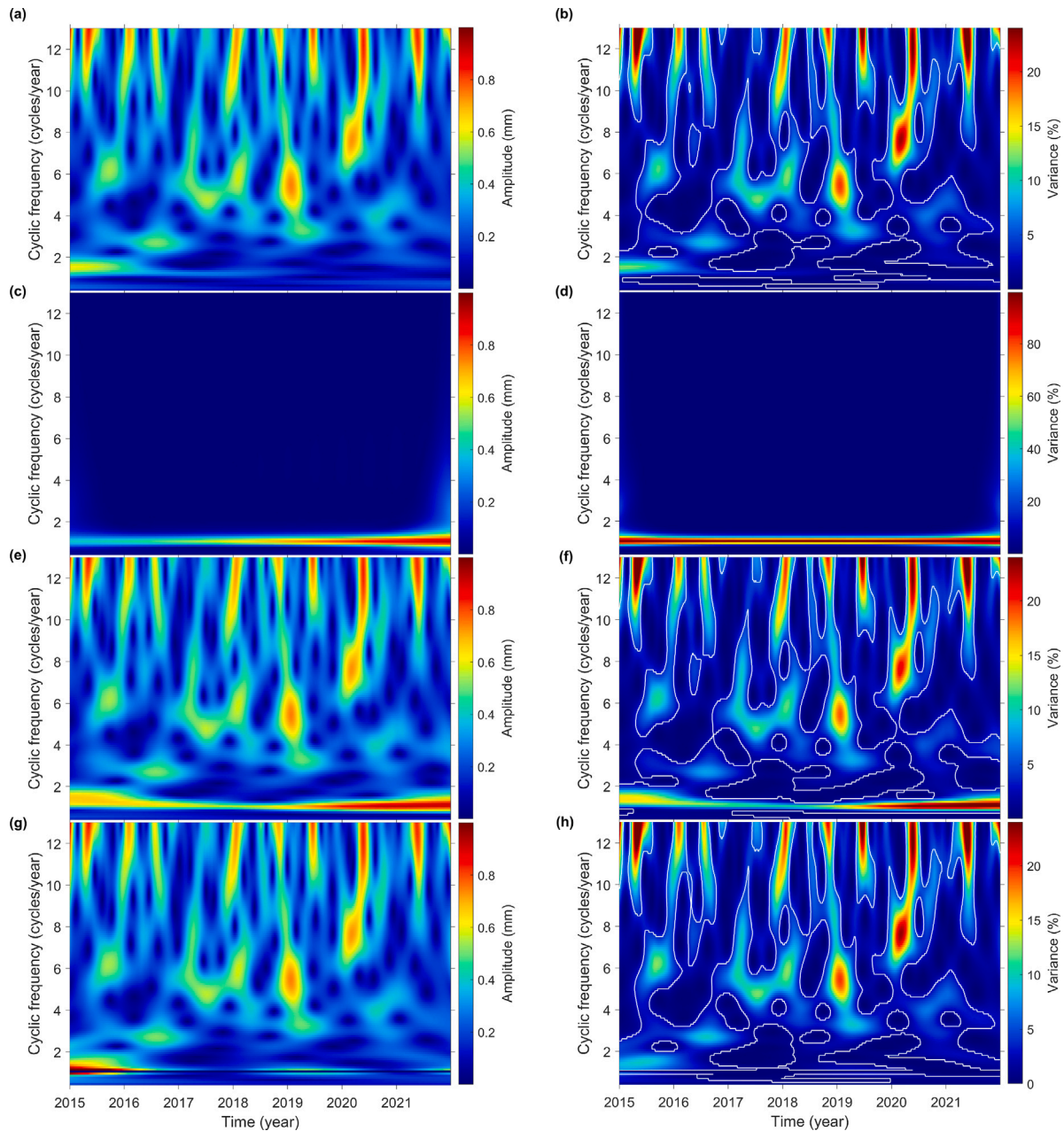
Fig. 3. The amplitude LSWSs (left panels) and normalized LSWSs (right panels) of: (a)–(b) the flicker and Gaussian white noise shown in Fig. 2(a)–(b), (c)–(d) the annual component shown in Fig. 2(c), (e)–(f) the simulated GNSS time series shown in Fig. 2(e), and (g)–(h) the simulated GNSS time series after suppressing annual peaks. The contour lines separate statistically significant peaks at 99% confidence level. The color bars are fixed to aid visualization, except for panel (d).

4.2. Velocity estimation before and after jump removal

Fig. 6 illustrates the estimated linear trends of GNSS time series considering their standard errors before (in red) and after (in blue) the jump removal. The LSSA tool in LSWAVE or JUST is applied to estimate the trend lines. The straight red line for each time series shown in Fig. 6 is obtained by fitting the linear trend constituents while the blue line is obtained after entering the jump indices and annual cyclic frequency in the LSSA software. In geodetic time series, such as very long baseline interferometry (VLBI) and GNSS time series, the velocity is usually constant for many years; however, jumps can occur due to many factors, such as earthquakes and antenna changes. In other words, all the linear pieces between the jumps usually have a consistent slope [5, Chapter 8]. Therefore, for each linear piece, an independent intercept is estimated, but a unique slope is estimated for all the pieces as illustrated in black in Fig. 6. This is also inline with the

trend estimates provided at http://www.epncb.oma.be/ (Last accessed on 24/09/2023).

The estimated intercept and slope of the linear trend and amplitude of the annual component for each time series are listed in Table 2. The estimated velocity using method B is more in agreement with the estimated velocity by Tunini et al. [41]. However, method B has relatively smaller estimated errors. It is worthwhile mentioning that through simulation, it is also shown that simultaneous seasonal-trend fit can estimate the slope (velocity) more accurately than the simple linear regression, e.g., [12, Section 3.5] and [47, Section VII].

4.3. Stochastic confidence level surfaces for two cases

The 3D and 2D views of a stochastic surface at 99% confidence level for the GNSS time series are illustrated in Fig. 8, respectively. Panels
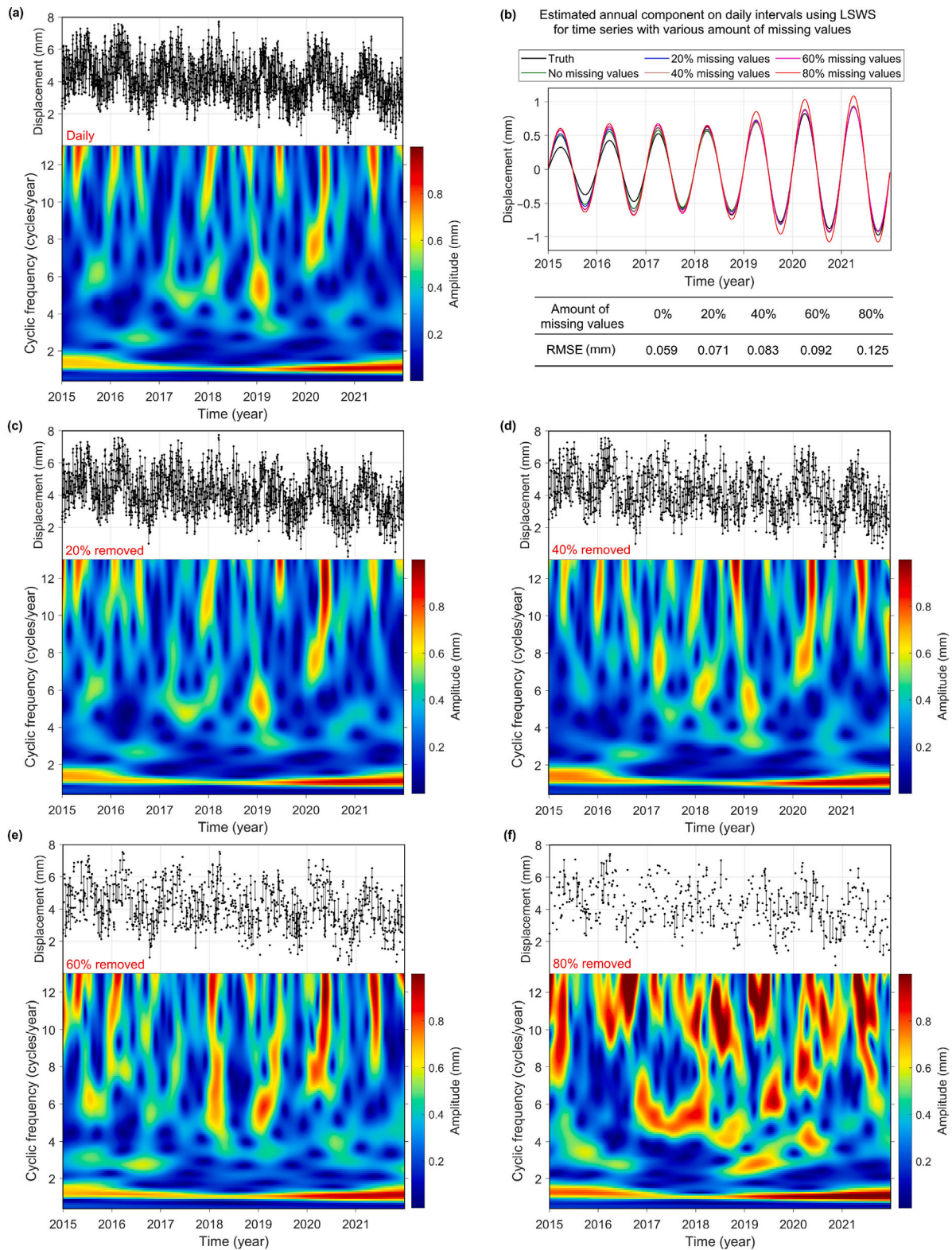
Fig. 4. The amplitude spectrograms of the simulated position time series for different amount of missing values.

(a) and (b) are calculated based on the windows of fixed size at each cyclic frequency translated over time stamps of the GNSS time series. The gaps in the stochastic surface, appeared as the vertical blank lines in Fig. 8(b) particularly in years 2005, 2006, and 2020, are due to the missing measurements in the GNSS time series (Fig. 7). This is for the case when users want to compute the critical variances only at the times when there are measurements.

Fig. 8(c) and (d) respectively show the 3D and 2D views of a stochastic surface for the GNSS time series when daily regular time stamps are considered as described in Section 2.4. One can observe
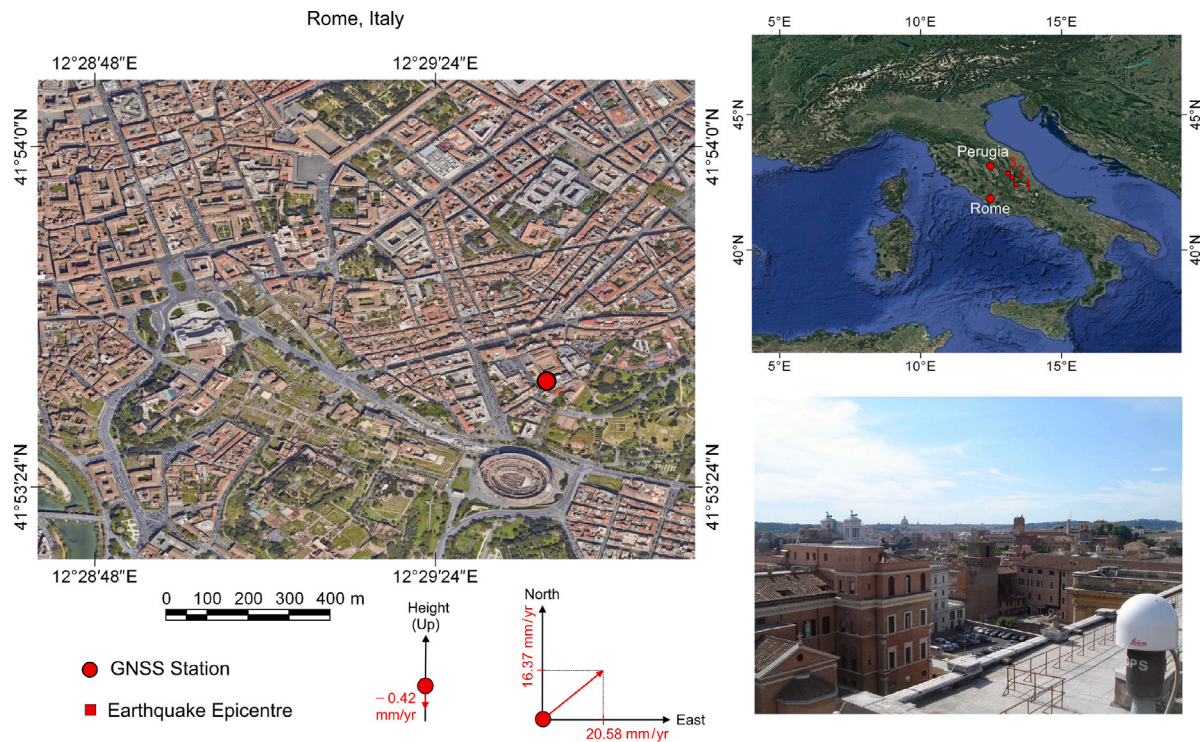
Fig. 5. The geographic location of the GNSS station in Rome, Italy. The maps are produced by the authors using Google Satellite in QGIS. More photos taken by camera are available at https://network.igs.org/M0SE00ITA (Last accessed on 24/09/2023). The red squares in the top right map show the epicenters of L'Aquila, Amatrice, Norcia earthquakes, respectively.

Table 2
The estimated linear trend and annual components of the GNSS time series shown in Fig. 6 at 99% confidence level. Method A is simple linear trend fit considering the measurement errors but without jump correction. Method B is the simultaneous seasonal-trend fit considering the jumps and measurement errors. The intercepts are the estimated differences between the position on 15/10/2004 and the NEU reference position, estimated from the centralized GNSS time series.

Direction	Method	Intercept (mm)	Velocity (mm/year)	Annual amplitude (mm)
North	A	-142.529 ± 0.037	16.003 ± 0.004	
	B	-143.655 ± 0.026	16.374 ± 0.003	1.198 ± 0.018
	Tunini et al. [41]		16.500 ± 0.080	
East	A	-180.408 ± 0.041	20.228 ± 0.004	
	B	-179.755 ± 0.024	20.579 ± 0.002	1.072 ± 0.018
	Tunini et al. [41]		20.870 ± 0.100	
Up	A	2.615 ± 0.110	-0.305 ± 0.011	
	B	-2.382 ± 0.070	-0.421 ± 0.007	1.503 ± 0.051
	Tunini et al. [41]		-0.410 ± 0.180	

that the critical variances increase as the window size decreases. Note that the calculation of this surface is based on the windows of fixed length at each cyclic frequency translated over equally spaced daily time stamps. Thus, since the window size may change when there are missing values, the critical variance can further increase as it is more evident in years 2005, 2006, and 2020 when there are more missing measurements (see Fig. 8(d)). This is for the case when users want to compute the critical variances for daily spaced time stamps. In the following section, this stochastic surface is used. In other words, a spectrogram on daily spaced time stamps is estimated for each GNSS time series and if spectral peaks stand above the stochastic surface in Fig. 8(c), then they are significant at 99% from the statistical point of view.

4.4. The least-squares wavelet analysis of GNSS time series

In this section, LSWA of the NEU GNSS time series are presented. In Figs. 9 and 10, the panel below each time series shows its corresponding time–frequency spectrogram (LSWS). First to see the potential effect of considering measurement errors (uncertainties) in the estimation

of spectrogram, LSWSs of the height time series without and with considering the measurement errors are illustrated in Fig. 9(a) and (b), respectively. Note that the jumps are not removed in Fig. 9. The peaks with relatively higher variance within white contour curves are statistically significant at 99% confidence level. In other words, these peaks stand above the stochastic surface shown in Fig. 8(c). Note that the stochastic confidence level surface for all these spectrograms are identical. However, some of the spectral peaks become statistically significant or insignificant when the measurement errors are considered. To aid the comparison, the spectral peaks at 1 cycle/year (annual) and 6 cycles/year are illustrated in Fig. 9(c) and (d), respectively, which are the cross-sections of spectrograms shown in Fig. 9(a) and (b) and Fig. 10(c). The annual peaks are statistically significant in all years, but they are less significant from 2013 to 2015 and much less significant after 2018. The spectral peaks with cyclic frequencies higher than 6 cycles/year observed toward the end of 2016 in the spectrogram of the height time series may probably be due to the effect of Norcia earthquake that remained statistically significant with or without considering measurement errors and even after the jump
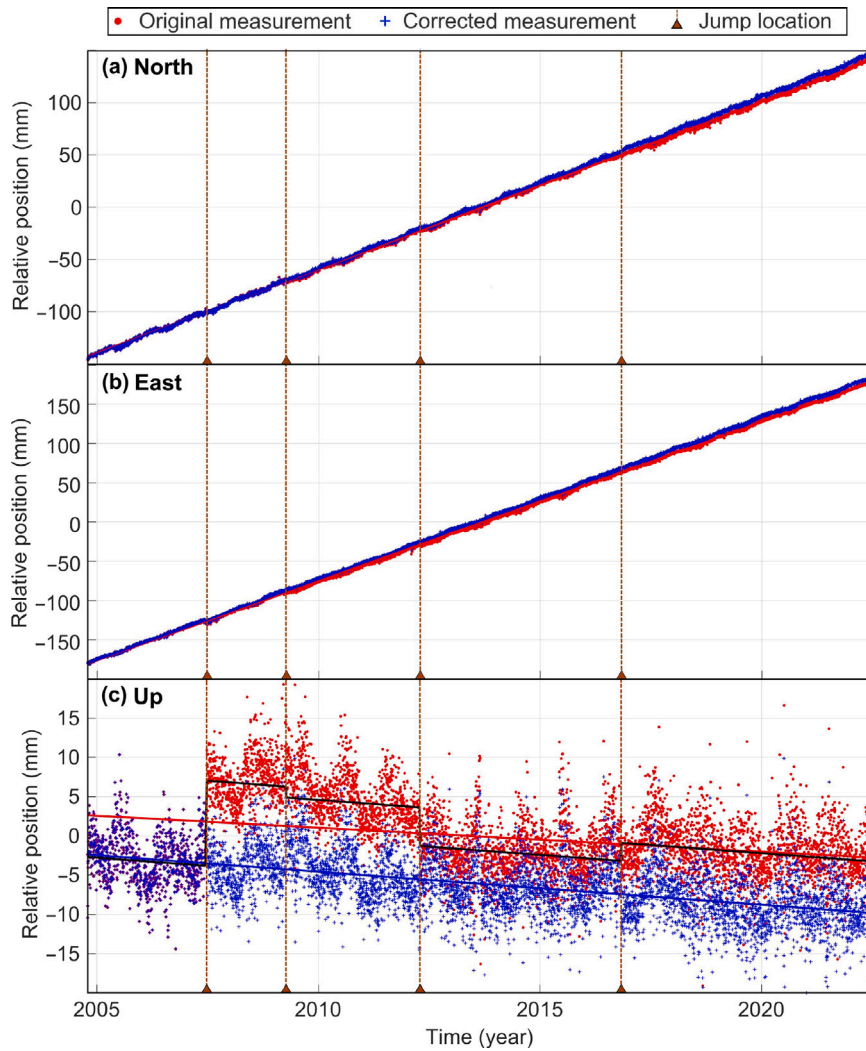
Fig. 6. The NEU GNSS time series and their estimated linear trends before (in red) and after the jump removal (in blue). The estimated linear trend of five pieces with a fix slope (velocity), used to correct the time series, is shown in black. The vertical dashed lines show the jump locations.
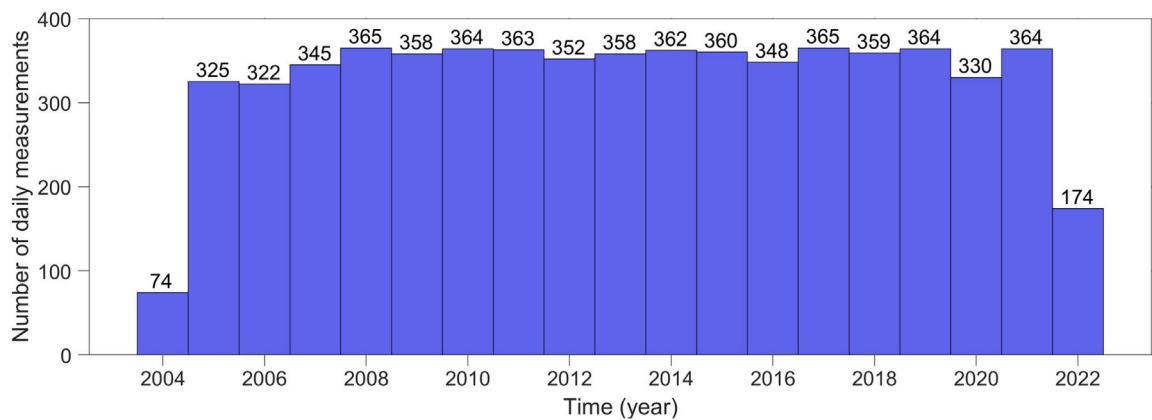

Fig. 7. A bar chart showing the number of available daily measurements for each year.

removal as illustrated in Fig. 10(c). This is investigated further in the discussion section.

The NEU time series along with their standard errors after removing the trend line of five pieces, shown by black lines in Fig. 6, are illustrated in Fig. 10. Their corresponding LSWSs are also shown in the panels below them. It is evident that the annual peaks are statistically significant in all the three time series. The percentage variance of the annual peaks in the height time series after 2018 are much lower than the ones in the east time series. Considering appropriate weight matrices in LSWA can significantly improve the estimation of spectral peaks in spectrogram [10,48]. Fig. 10(d) shows LSWS by considering a fully populated covariance matrix based on adjusted white noise
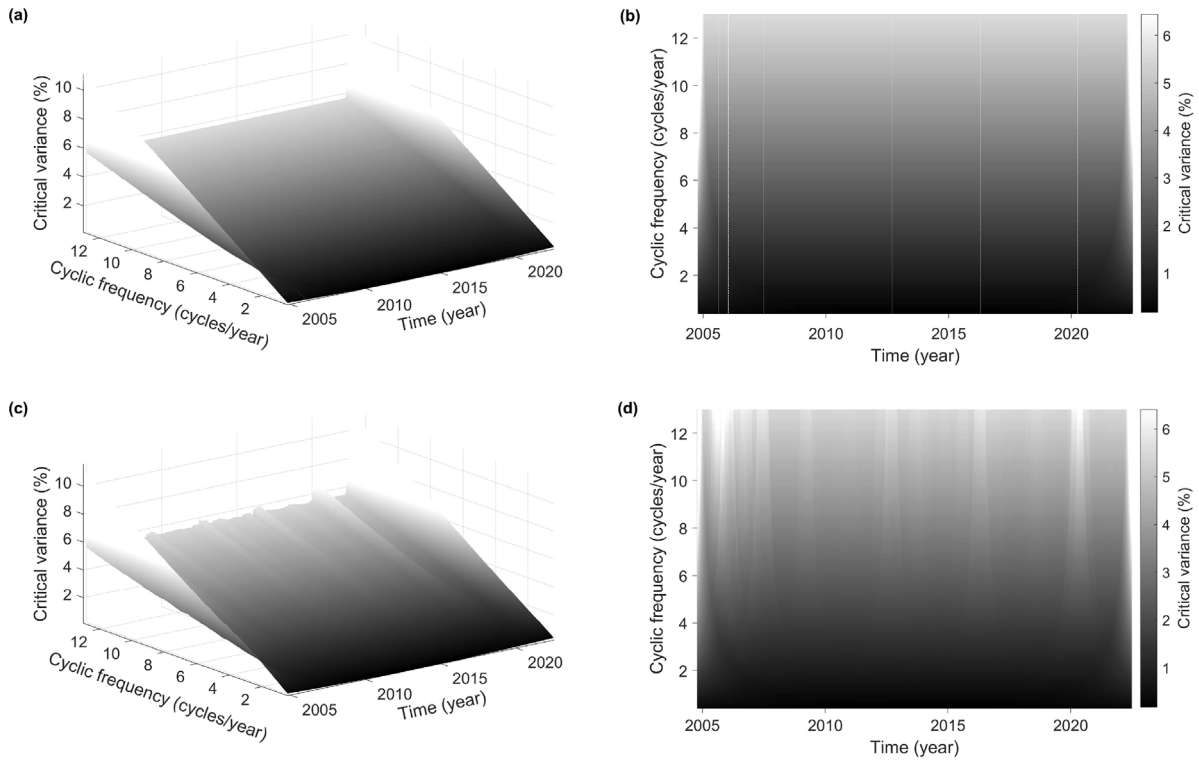
(a)

(b)

(c)

(d)

Fig. 8. The 3D and 2D representation of the stochastic surfaces at 99% confidence level, (a) and (b) when the critical values are estimated for the input time–frequency grid, where the times are the times of measurements, and (c) and (d) when the critical values are estimated for the regular time–frequency grid, i.e., daily time stamps.

and flicker noise from the techniques described in [32,49]. Comparing panels (c) and (d), one can observe a significant reduction in the percentage variance of the spectral peaks.

4.5. The least-squares wavelet analysis of InSAR time series

Normalized spectrograms and linear trends are estimated for the part of GNSS time series from 2018 and the EGMS Ortho-Vertical time series (2018–2022). The results are illustrated in Fig. 11. Both time series show a declining trend but with slightly different velocities. The percentage variance of the annual peaks increases over time as can be observed in both LSWSs displayed in Fig. 11(a) and (b), while the spectral peaks at higher frequencies have irregular patterns. These peaks are likely due to flicker noise, atmospheric noise, and errors caused during the preprocessing including phase-unwrapping that are discussed further in the following sections. Overall, the trend results and annual peaks almost agree in both time series.

5. Discussion

5.1. Weight matrices and stochastic surfaces in LSWA

Pagiatakis discussed the stochastic significance of spectral peaks in LSS in two cases, covariance matrix with known and unknown a-priori variance factor [6]. In the case of known a-priori variance factor, the random variables Q_n and Q_s in Eq. (16) are distributed as the chi-square distribution, while in the case of unknown a-priori variance factor, the a-posteriori variance factor is estimated from the data, and so the random variables Q_n and Q_s follow the Fisher distribution. Whether the a-priori or a posteriori variance factor is used, it will be canceled out from the ratio in Eq. (7), and so this factor has no effect of the estimation of spectral peak. However, from the statistical point of view, the spectral peak should be slightly stronger (taller) to be statistically significant at the same confidence level. From [6, Figs. 4 and 5], it can be deduced that if a spectral peak is statistically significant at 99%

confidence level for the case of known a-priori variance factor, then the peak is also statistically significant at 95% confidence level whether the variance factor is known or unknown for all segment sizes. If the segment size is larger than 150, then the critical percentage variances are almost identical for known and unknown variance factor scenarios. In the present study, the GNSS segment sizes at the maximum estimated cyclic frequency of 12 (cycles/year) roughly include 180 measurements as 6 cycles are used within each window, so the stochastic significance of the estimated peaks at 99% are independent of the choice of which variance factor is used in the calculation of the covariance matrix of the estimated parameters.

Though the variance factor does not have any influence on the spectral peaks estimated by Eq. (16), the relative weights assigned to measurements within each window can make a significant difference. In the present study, at each cyclic frequency, the weight matrix $\mathbf{P_y}$ associated with segment $\mathbf{y}$ was obtained by the Gaussian values multiplied by the inverse of squared errors which empirically metricized each segment. Theoretically, the weight matrix is diagonal and positive definite, and so all the derivations shown in Section 2 remain valid. The weight matrices play a crucial role in estimating trend and spectral components and in searching for hidden signatures [10]. Ghaderpour et al. [48, Appendix 1] also showed the advantages of considering fully and partially populated weight matrices in estimating the spectral peaks in LSWS through experiments.

5.2. Effect of jumps, noises, and missing values in signal estimation

Another crucial factor that may significantly bias the trend and spectral estimations is systematic noise, e.g., the presence of jumps or discontinuities. It was shown in Figs. 6, 9 and 10 that accurate jump removal plays a crucial role in robustly estimating the trend and spectral components of the GNSS time series. The locations of the significant jumps due to antenna changes on the 19/06/2007 and 13/04/2012 in the position time series were known in the GNSS time series analyzed in this research. The other two jumps on the
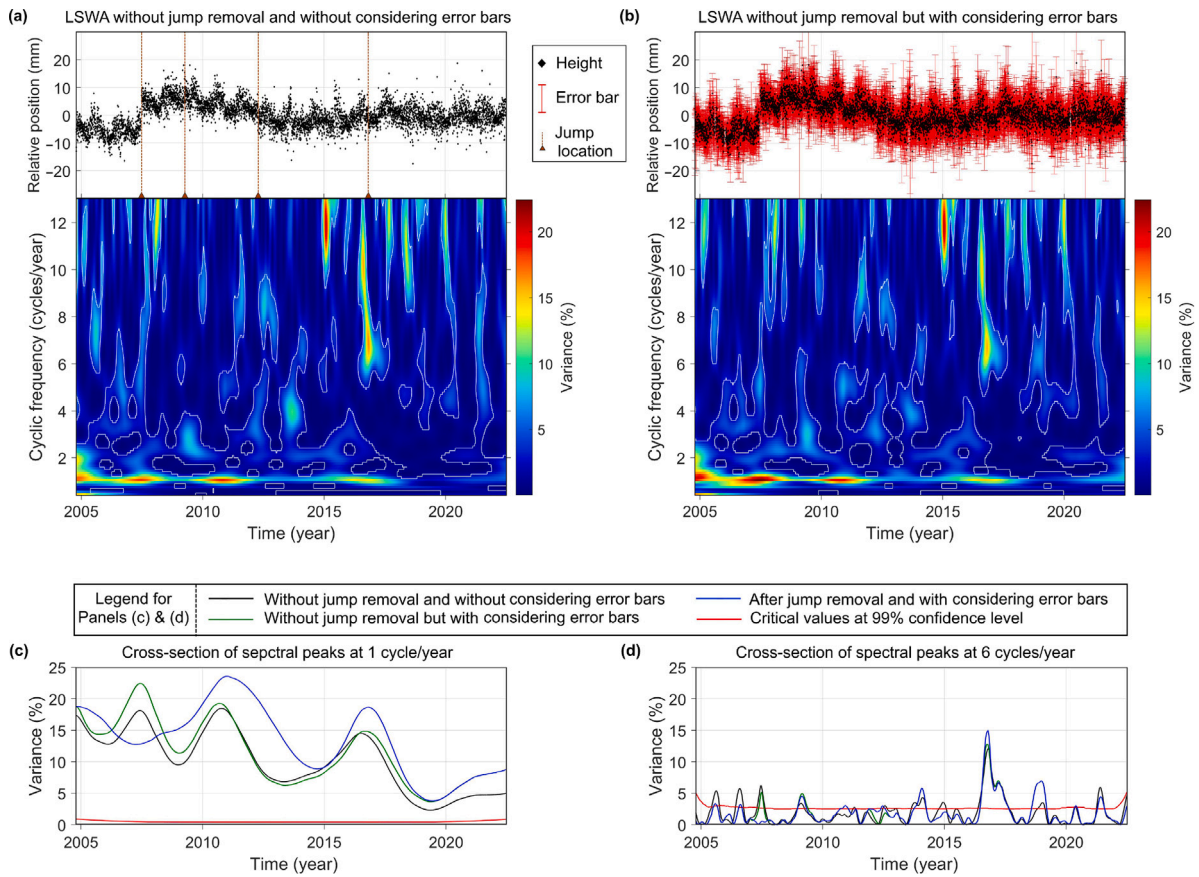
Fig. 9. The analysis of height (up) time series after removing the linear trend without jump removal: (a) without considering measurement errors, and (b) with considering measurement errors. The panels with the jet color bars are spectrograms. The contour lines separate the statistically significant peaks at 99% confidence level. Panels (c) and (d) show the spectral peaks at 1 cycle/year and 6 cycles/year, respectively, obtained from the cross-sections of spectrograms in panels (a) and (b) and Fig. 10(c). The red lines in panels (c) and (d) are respectively the cross-sections of the stochastic confidence level surface at 1 cycle/year and 6 cycles/year, shown in Fig. 8(d).

08/04/2009 and 30/10/2016 had a lower bias on trend and spectral estimations. It is worth mentioning that the JUSTjumps tool in JUST can also be used for efficiently detecting jump locations in a time series when they are unknown [14]. Table 1 demonstrated the robustness of weighted LSWA for estimating signals for different noise levels and number of missing values. Generally, in the presence of noise, the higher the number of missing values, the lower the accuracy of signal estimation. Comparing the RMSEs of ordinary LSWA and weighted LSWA in Table 1 shows that appropriate weights assigned to noisy measurements (the case of weighted LSWA) provided a robust signal estimation.

5.3. Flicker noise observed in GNSS position time series

It is known that GNSS position time series contains colored noise (flicker noise or pink noise) and white noise; however, the source of such intrinsic noise is still unclear [49–52]. For example, Rebischung et al. [53] discussed that real crustal displacements generated by non-tidal loading deformations is another contributor to the flicker noise. Likewise, InSAR displacement time series also present colored noise due to several factors, such as errors caused during phase-unwrapping and atmospheric noise [39,45,46]. Note that the high frequency peaks may not always represent sensor noise, and it could potentially explain a geophysical mechanism.

The LSWS of height time series shown in Fig. 10(c) presented many aperiodic signatures. In particular, the spectrogram of the height time series showed statistically significant spectral peaks during August to December 2016. There is a possibility that Amatrice and Norcia earthquakes in 2016 might have contributed to these high frequency

peaks. To verify possible origins of these peaks, LSSA was applied to the segment of the height time series from August to December 2016 (four-month duration). The LSS detected a peak at 6.7 cycles/year that matched the most significant peak illustrated in Fig. 10(c). The estimated amplitude of the sinusoids corresponding to this peak at 6.7 cycles/year was 2.21 ± 0.32 mm.

There are other agencies who provide GNSS time series for the same station (M0SE). For example, EUREF Permanent Network (EPN) Central Bureau https://epncb.oma.be/ (Last accessed on 01/01/2024) provides the residual GNSS height time series, and Nevada Geodetic Laboratory http://geodesy.unr.edu/ (Last accessed on 01/01/2024) provides GNSS height time series for the same station. Fig. 12 illustrates LSWSs of these time series using the same input parameters (jump locations and window size parameters) as for estimating LSWS in Fig. 10(c) with a fixes color bar to aid visualization. Comparing Fig. 10(c) with Fig. 12, one can clearly observe the irregular patterns for the spectral peaks at high frequencies. These differences most likely indicate positioning errors specific to the particular GNSS height time series used.

Furthermore, the annual cycles of the NEU time series were less significant between years 2018 and 2021 as seen in Figs. 10 and 12. To further investigate whether the spectral peaks in year 2016 as observed in Fig. 10(c), magnified in Fig. 13(a) are linked to the Amatrice and Norcia earthquakes, another GNSS height time series located in Perugia was also analyzed by LSWA. The geographic location of this GNSS station is also displayed in Fig. 5. The LSWS of this GNSS time series does not have any statistically significant peak at any frequencies from 6 to 12 cycles/year, see Fig. 13(b). Fig. 13(c) and (d) show the magnified sections of the LSWSs in Fig. 12 which indicates that the spectral peak at 6.7 cycles/year in Oct-Nov 2016 are likely due to positioning errors
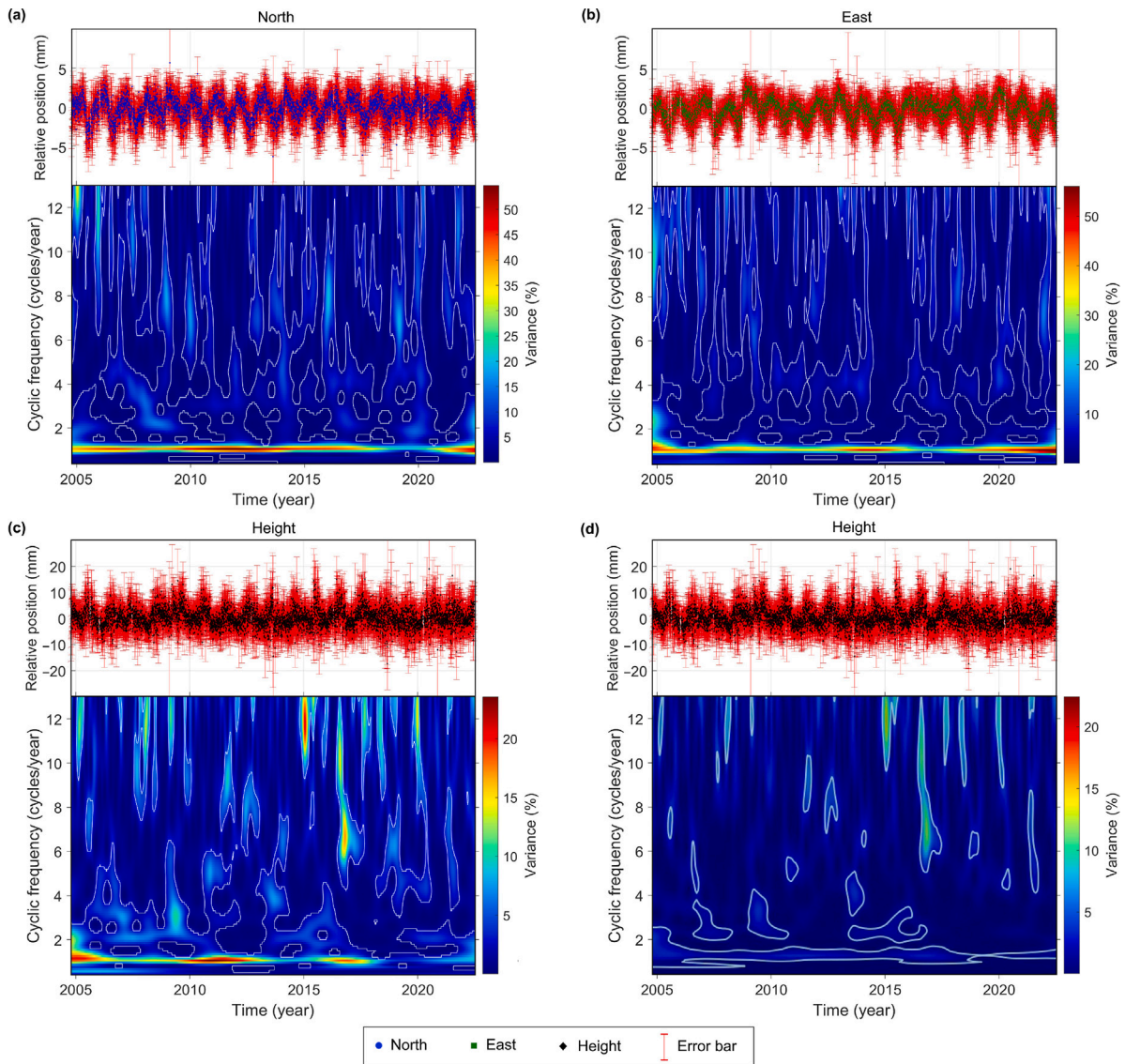
Fig. 10. (a)–(c) The LSWA results of north, east, and height (up) GNSS time series after jump and trend removal considering measurement errors, and (d) The LSWA results using a fully populated covariance matrix instead of a diagonal matrix. The contour lines separate the statistically significant peaks at 99% confidence level.
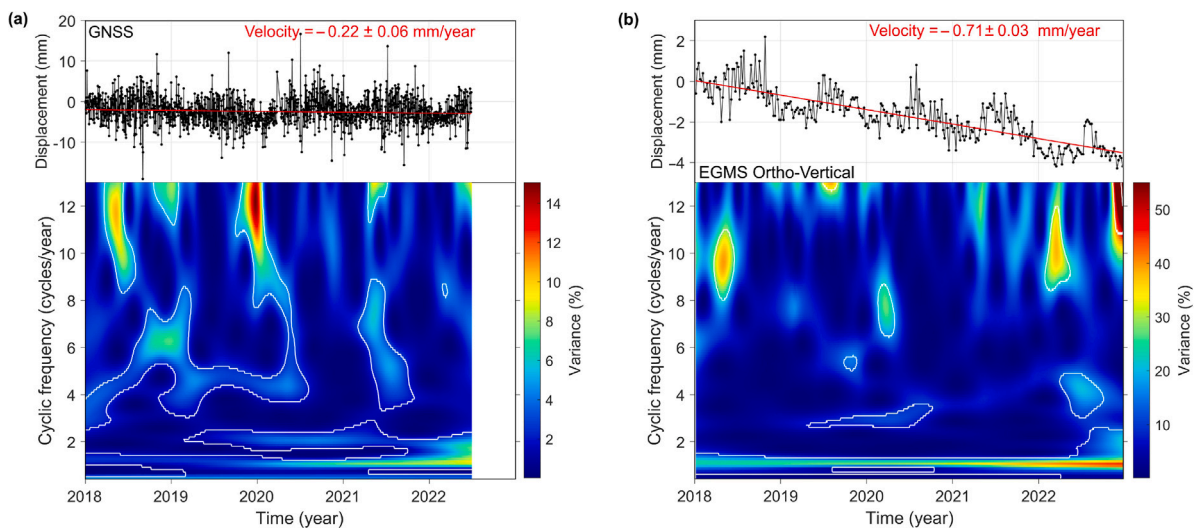

Fig. 11. The trend analysis and LSWA for (a) GNSS time series, and (b) EGMS Ortho-Vertical time series. The white contour lines surround parts of the spectrogram found to be statistically significant at 99% confidence level.
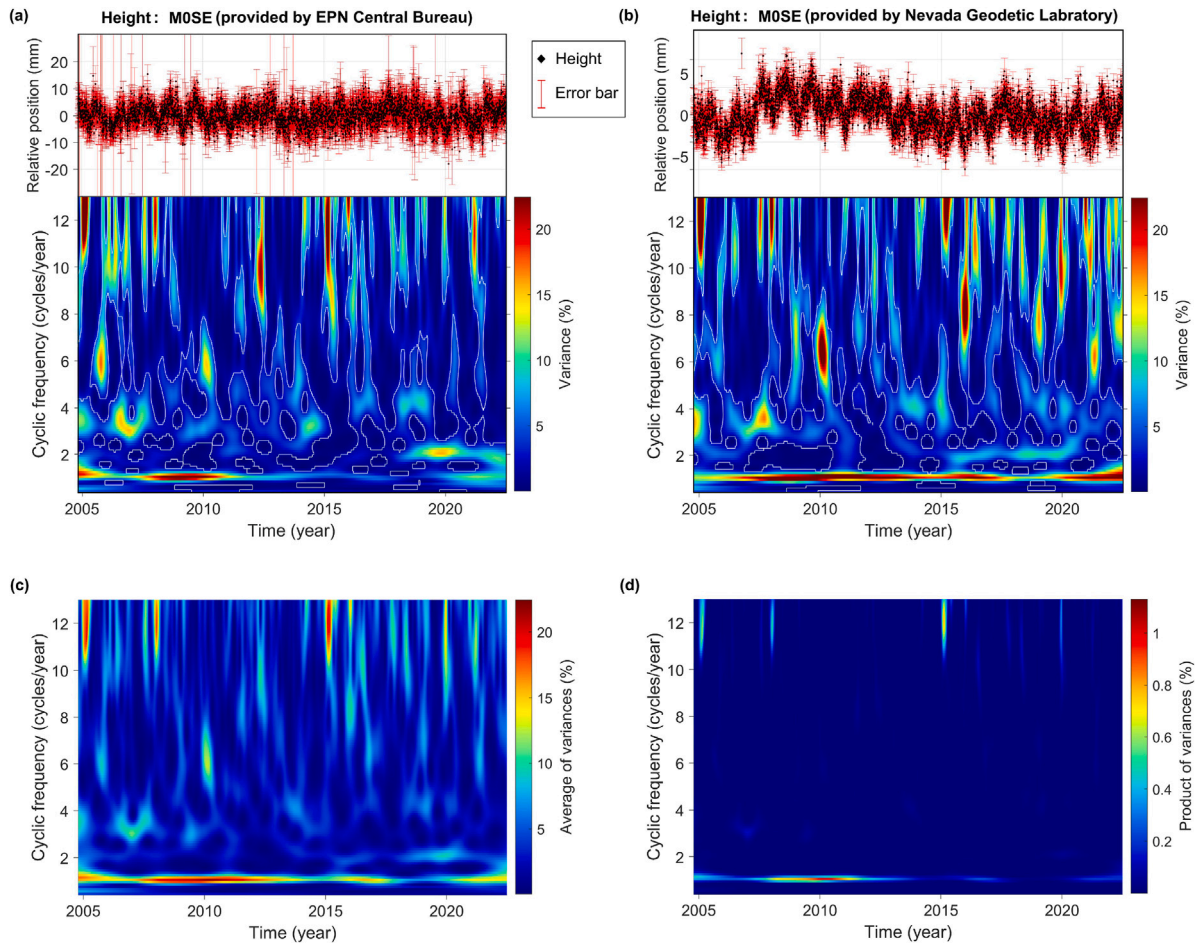
Fig. 12. The LSWA results of the GNSS height time series for M0SE00ITA provided by (a) EPN Central Bureau and (b) Nevada Geodetic Laboratory after jump and trend removal considering measurement errors with the same window size parameters and jump locations as for Fig. 10(c). The contour lines separate the statistically significant peaks at 99% confidence level. Panels (c) and (d) show the spectrograms obtained by entrywise averaging and multiplying of the spectrograms displayed in panels (a), (b), and Fig. 10(c).

and modeling rather than seismic noise. Employing a fully populated covariance matrix based on adjusted white and flicker noises in LSWA instead of a diagonal matrix could potentially improve the estimation of spectral peaks in the spectrograms as shown in Fig. 10(d), though the computational cost can significantly increase.

The GNSS height time series provided by the three different agencies for the same station show different seasonal patterns across the time–frequency domain. To better visualize this, the spectrograms in Fig. 10(c), Fig. 12(a) and (b), with the same input parameters and dimensions, are entrywise averaged to display in Fig. 12(c) and entrywise multiplied to display in Fig. 12(d). The entrywise averaging (multiplying) in this context means that the variances of spectral peaks corresponding to the same pair of time and frequency in the three spectrograms are being averaged (multiplied). Fig. 12(d), motivated by the cross-wavelet transform [11], clearly shows the annual peaks are dominant and more significant in 2010 for all three time series. Likewise, short duration monthly peaks (12 cycles/year) in 2005 and 2015 are more dominant in all the three time series. As discussed in [22,33,54], seasonal peaks observed in GNSS measurements could be due to several reasons, such as thermal deformation, hydrological loading, as well as error in modeling and sensors. Therefore, it is crucial to understand and handle the uncertainties in the measurements and models first before investigating the potential geophysical mechanisms that cause the components of GNSS time series. Models like the Least-Squares Cross-Wavelet Analysis (LSCWA) [13,39,40] could also be useful to investigate the potential coherency and phase delay between components of GNSS time series and other time series, such as

air pressure, temperature, and groundwater that are subject to future investigation.

6. Conclusions

In this research, the mathematical derivation of the stochastic confidence level surface for the least-squares wavelet spectrogram was presented. A simulation experiment was carried out to demonstrate the robustness of LSWA for signal estimation in presence of noises and missing values. The stochastic significance of peaks in the spectrogram for cases of empirical and statistical weights was demonstrated for GNSS position time series in Rome, Italy. It was shown that the critical variance depends on the window size which increases as window size decreases, indicating that the percentage variance of spectral peaks at higher frequencies must be higher to be significant from statistical point of view. It was demonstrated that ignoring the jumps due to antenna change and earthquake can significantly bias spectrograms and trend estimations. Therefore, considering measurement errors as well as jump removal are crucial for a more robust seasonal-trend estimation. All the three GNSS components (north, east, up) contained annual components likely linked to hydrological loading and/or thermal deformation. The results of the EGMS Ortho-Vertical time series showed a similar annual cycle pattern and a declining trend as the GNSS height time series during 2018–2022. The LSWSs of the GNSS height time series from three different agencies were also compared in this research and their joint spectrograms showed dominant annual cycles, more significant in 2010 and less significant from 2018 to 2020. Future studies shall focus on investigating possible origins of annual and semi-annual cycles and flicker noise in the GNSS position time series.
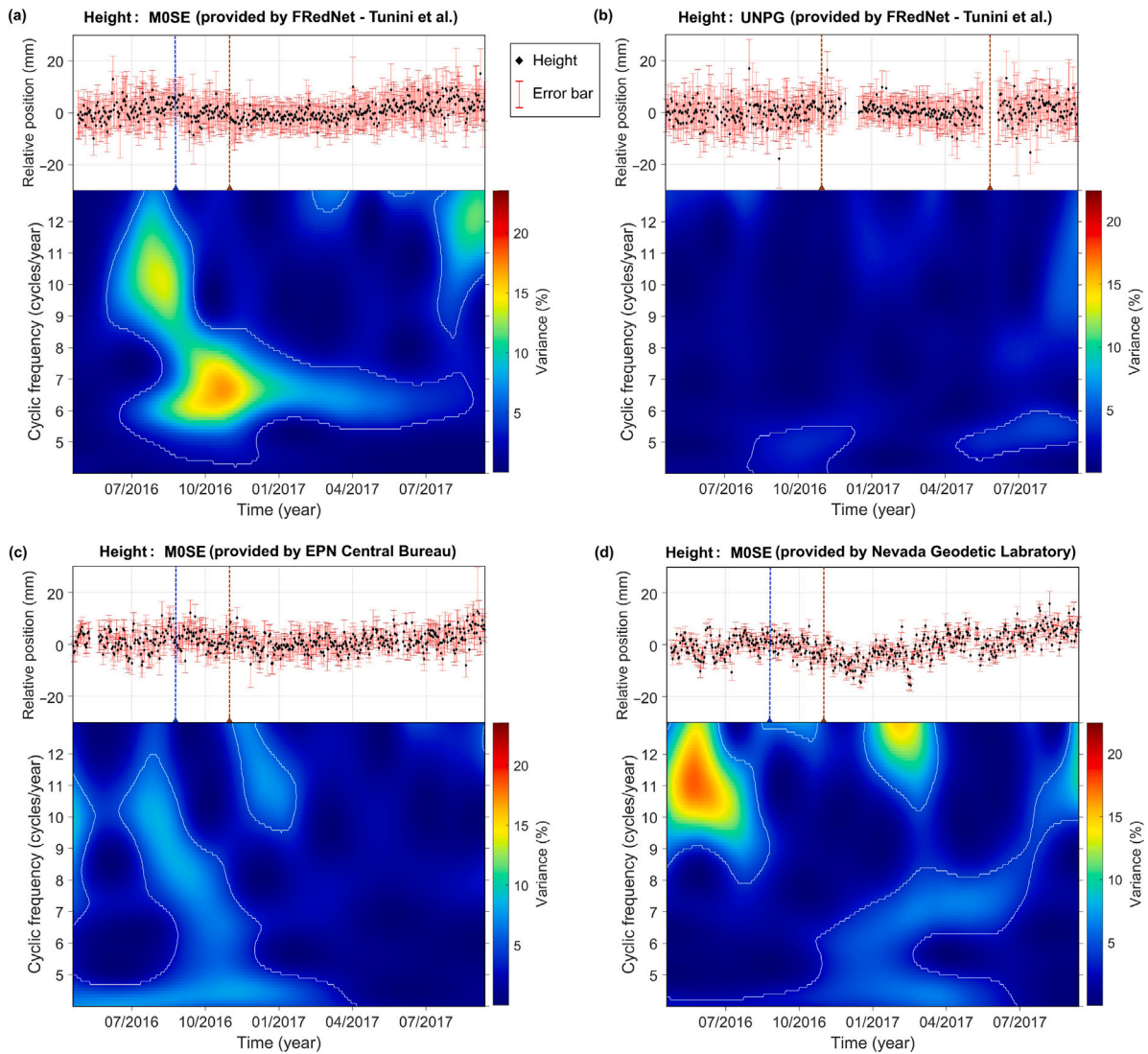
Fig. 13. (a) A magnified section of LSWS illustrated in Fig. 10(c), (b) the LSWS of the height time series of GNSS receiver with ID: UNPG00ITA in Perugia, Italy, (c)–(d) magnified sections of LSWSs illustrated in Fig. 12(a) and (b), respectively. The contour lines separate the statistically significant peaks at 99% confidence level. The vertical dashed lines show the locations of jumps or discontinuities. The blue dashed line shows the location of a disturbance due to Amatrice earthquake on August 24, 2016, and the brown dashed line on October 30, 2016, shows the location of a jump due to Norcia earthquake. The discontinuity on May 24, 2017, in panel (b) is also due to antenna changes.

CRediT authorship contribution statement

Ebrahim Ghaderpour: Writing – original draft, Visualization, Validation, Software, Methodology, Investigation, Formal analysis, Data curation, Conceptualization. **Spiros D. Pagiatakis:** Writing – review & editing, Conceptualization. **Gabriele Scarascia Mugnozza:** Writing – review & editing, Conceptualization. **Paolo Mazzanti:** Writing – review & editing, Conceptualization.

Declaration of competing interest

The authors declare that they have no known competing financial interests or personal relationships that could have appeared to influence the work reported in this paper.

Data availability

Data will be made available on request.

Acknowledgments

Funding

Appendix

In this Appendix, it is proven that Eq. (7) can be written as Eq. (15). First note that from Eq. (3), $\underline{\mathbf{J}} = \underline{\boldsymbol{\Phi}}\, \underline{\mathbf{N}}^{-1} \underline{\boldsymbol{\Phi}}^T \mathbf{P_y}$, and $\underline{\mathbf{N}} = \underline{\boldsymbol{\Phi}}^T \mathbf{P_y} \underline{\boldsymbol{\Phi}}$, one can

write

$$\overline{\boldsymbol{\Phi}}^{\mathrm{T}}\mathbf{P_y}\underline{\mathbf{J}} = \begin{bmatrix} \boldsymbol{\Phi}^{\mathrm{T}}\mathbf{P_y}\underline{\boldsymbol{\Phi}} \ \underline{\mathbf{N}}^{-1}\underline{\boldsymbol{\Phi}}^{\mathrm{T}}\mathbf{P_y} \\ \underline{\boldsymbol{\Phi}}^{\mathrm{T}}\mathbf{P_y}\underline{\boldsymbol{\Phi}} \ \underline{\mathbf{N}}^{-1}\underline{\boldsymbol{\Phi}}^{\mathrm{T}}\mathbf{P_y} \end{bmatrix} = \begin{bmatrix} \boldsymbol{\Phi}^{\mathrm{T}}\mathbf{P_y} \\ \underline{\boldsymbol{\Phi}}^{\mathrm{T}}\mathbf{P_y}\underline{\boldsymbol{\Phi}} \ \underline{\mathbf{N}}^{-1}\underline{\boldsymbol{\Phi}}^{\mathrm{T}}\mathbf{P_y} \end{bmatrix}, \quad (24)$$

and then using Eq. (8), one can obtain

$$\overline{\mathbf{N}}^{-1}\overline{\boldsymbol{\Phi}}^{\mathrm{T}}\mathbf{P_y}\underline{\mathbf{J}}$$

$$= \begin{bmatrix} \mathbf{M_1} & \mathbf{M_2} \\ \mathbf{M_3} & \mathbf{M_4} \end{bmatrix} \begin{bmatrix} \boldsymbol{\Phi}^{\mathrm{T}}\mathbf{P_y} \\ \underline{\boldsymbol{\Phi}}^{\mathrm{T}}\mathbf{P_y}\underline{\boldsymbol{\Phi}} \ \underline{\mathbf{N}}^{-1}\underline{\boldsymbol{\Phi}}^{\mathrm{T}}\mathbf{P_y} \end{bmatrix} \quad (25)$$

$$= \begin{bmatrix} \mathbf{M_1}\underline{\boldsymbol{\Phi}}^{\mathrm{T}}\mathbf{P_y} + \mathbf{M_2}\boldsymbol{\Phi}^{\mathrm{T}}\mathbf{P_y}\underline{\boldsymbol{\Phi}} \ \underline{\mathbf{N}}^{-1}\underline{\boldsymbol{\Phi}}^{\mathrm{T}}\mathbf{P_y} \\ \mathbf{M_3}\underline{\boldsymbol{\Phi}}^{\mathrm{T}}\mathbf{P_y} + \mathbf{M_4}\boldsymbol{\Phi}^{\mathrm{T}}\mathbf{P_y}\underline{\boldsymbol{\Phi}} \ \underline{\mathbf{N}}^{-1}\underline{\boldsymbol{\Phi}}^{\mathrm{T}}\mathbf{P_y} \end{bmatrix}$$

$$= \begin{bmatrix} \left(\underline{\mathbf{N}}^{-1} + \underline{\mathbf{N}}^{-1}\underline{\boldsymbol{\Phi}}^{\mathrm{T}}\mathbf{P_y}\boldsymbol{\Phi} \ \mathbf{M_4} \ \boldsymbol{\Phi}^{\mathrm{T}}\mathbf{P_y}\underline{\boldsymbol{\Phi}} \ \underline{\mathbf{N}}^{-1}\right)\underline{\boldsymbol{\Phi}}^{\mathrm{T}}\mathbf{P_y} - \underline{\mathbf{N}}^{-1} \ \underline{\boldsymbol{\Phi}}^{\mathrm{T}}\mathbf{P_y}\boldsymbol{\Phi} \ \mathbf{M_4}\boldsymbol{\Phi}^{\mathrm{T}}\mathbf{P_y}\underline{\boldsymbol{\Phi}} \ \underline{\mathbf{N}}^{-1}\underline{\boldsymbol{\Phi}}^{\mathrm{T}}\mathbf{P_y} \\ -\mathbf{M_4} \ \boldsymbol{\Phi}^{\mathrm{T}}\mathbf{P_y}\underline{\boldsymbol{\Phi}} \ \underline{\mathbf{N}}^{-1}\underline{\boldsymbol{\Phi}}^{\mathrm{T}}\mathbf{P_y} + \mathbf{M_4}\boldsymbol{\Phi}^{\mathrm{T}}\mathbf{P_y}\underline{\boldsymbol{\Phi}} \ \underline{\mathbf{N}}^{-1}\underline{\boldsymbol{\Phi}}^{\mathrm{T}}\mathbf{P_y} \end{bmatrix}$$

$$= \begin{bmatrix} \underline{\mathbf{N}}^{-1}\underline{\boldsymbol{\Phi}}^{\mathrm{T}}\mathbf{P_y} \\ \mathbf{0} \end{bmatrix}. \quad (26)$$

Therefore,

$$\overline{\mathbf{J}}\underline{\mathbf{J}} = \overline{\boldsymbol{\Phi}} \ \overline{\mathbf{N}}^{-1}\overline{\boldsymbol{\Phi}}^{\mathrm{T}}\mathbf{P_y}\underline{\mathbf{J}} = \begin{bmatrix} \underline{\boldsymbol{\Phi}} & \boldsymbol{\Phi} \end{bmatrix} \begin{bmatrix} \underline{\mathbf{N}}^{-1}\underline{\boldsymbol{\Phi}}^{\mathrm{T}}\mathbf{P_y} \\ \mathbf{0} \end{bmatrix} = \underline{\boldsymbol{\Phi}} \ \underline{\mathbf{N}}^{-1}\underline{\boldsymbol{\Phi}}^{\mathrm{T}}\mathbf{P_y} = \underline{\mathbf{J}}. \quad (27)$$

Taking the transpose of both sides of Eq. (27), it can be seen that $\mathbf{P_y}\underline{\mathbf{J}}\overline{\mathbf{J}} = \mathbf{P_y}\underline{\mathbf{J}}$. Since $\overline{\mathbf{J}}\underline{\mathbf{J}} = \underline{\mathbf{J}}$ (Eq. (27)) and

$$\hat{\mathbf{g}}^{\mathrm{T}}\mathbf{P_y}\underline{\boldsymbol{\Phi}} = (\mathbf{y} - \underline{\mathbf{J}} \ \mathbf{y})^{\mathrm{T}}\mathbf{P_y}\underline{\boldsymbol{\Phi}}$$

$$= (\mathbf{y} - \underline{\boldsymbol{\Phi}} \ \underline{\mathbf{N}}^{-1}\underline{\boldsymbol{\Phi}}^{\mathrm{T}}\mathbf{P_y}\mathbf{y})^{\mathrm{T}}\mathbf{P_y}\underline{\boldsymbol{\Phi}}$$

$$= \mathbf{y}^{\mathrm{T}}(\mathbf{I} - \mathbf{P_y}\underline{\boldsymbol{\Phi}} \ \underline{\mathbf{N}}^{-1}\underline{\boldsymbol{\Phi}}^{\mathrm{T}})\mathbf{P_y}\underline{\boldsymbol{\Phi}}$$

$$= \mathbf{y}^{\mathrm{T}}(\mathbf{P_y}\underline{\boldsymbol{\Phi}} - \mathbf{P_y}\underline{\boldsymbol{\Phi}}) = \mathbf{0}, \quad (28)$$

it can be verified that

$$\hat{\mathbf{g}}^{\mathrm{T}}\mathbf{P_y}\overline{\mathbf{J}}\hat{\mathbf{g}} = \hat{\mathbf{g}}^{\mathrm{T}}\mathbf{P_y}\overline{\mathbf{J}}(\mathbf{y} - \underline{\mathbf{J}} \ \mathbf{y})$$

$$= \hat{\mathbf{g}}^{\mathrm{T}}\mathbf{P_y}\overline{\mathbf{J}}\mathbf{y} - \hat{\mathbf{g}}^{\mathrm{T}}\mathbf{P_y}\overline{\mathbf{J}}\underline{\mathbf{J}} \ \mathbf{y}$$

$$= \hat{\mathbf{g}}^{\mathrm{T}}\mathbf{P_y}\overline{\mathbf{J}}\mathbf{y} - \hat{\mathbf{g}}^{\mathrm{T}}\mathbf{P_y}\underline{\mathbf{J}} \ \mathbf{y}$$

$$= \hat{\mathbf{g}}^{\mathrm{T}}\mathbf{P_y}\overline{\mathbf{J}}\mathbf{y} - (\hat{\mathbf{g}}^{\mathrm{T}}\mathbf{P_y}\underline{\boldsymbol{\Phi}}) \ \underline{\mathbf{N}}^{-1}\underline{\boldsymbol{\Phi}}^{\mathrm{T}}\mathbf{P_y} \ \mathbf{y}$$

$$= \hat{\mathbf{g}}^{\mathrm{T}}\mathbf{P_y}\overline{\mathbf{J}}\mathbf{y}$$

$$= \hat{\mathbf{g}}^{\mathrm{T}}\mathbf{P_y}\overline{\boldsymbol{\Phi}} \ \hat{\overline{\mathbf{c}}}$$

$$= \hat{\mathbf{g}}^{\mathrm{T}}\mathbf{P_y}\underline{\boldsymbol{\Phi}} \ \mathbf{x} + \hat{\mathbf{g}}^{\mathrm{T}}\mathbf{P_y}\boldsymbol{\Phi} \ \hat{\mathbf{c}}$$

$$= \hat{\mathbf{g}}^{\mathrm{T}}\mathbf{P_y}\boldsymbol{\Phi} \ \hat{\mathbf{c}}$$

$$= \hat{\mathbf{g}}^{\mathrm{T}}\mathbf{P_y}\mathbf{J}\hat{\mathbf{g}}, \quad (29)$$

where the parameters are the same as the ones in Eq. (13). Therefore, Eq. (7) is identical to

$$s = \frac{\hat{\mathbf{g}}^{\mathrm{T}}\mathbf{P_y}\overline{\mathbf{J}}\hat{\mathbf{g}}}{\hat{\mathbf{g}}^{\mathrm{T}}\mathbf{P_y}\hat{\mathbf{g}}}. \quad (30)$$

Since $\overline{\mathbf{J}}$ and $\underline{\mathbf{J}}$ are idempotent and $\overline{\mathbf{J}}\underline{\mathbf{J}} = \underline{\mathbf{J}}$ and $\mathbf{P_y}\underline{\mathbf{J}}\overline{\mathbf{J}} = \mathbf{P_y}\underline{\mathbf{J}}$,

$$\hat{\mathbf{g}}^{\mathrm{T}}\mathbf{P_y}\overline{\mathbf{J}}\hat{\mathbf{g}} = (\mathbf{y} - \underline{\mathbf{J}} \ \mathbf{y})^{\mathrm{T}}\mathbf{P_y}\overline{\mathbf{J}}(\mathbf{y} - \underline{\mathbf{J}} \ \mathbf{y})$$

$$= \mathbf{y}^{\mathrm{T}}(\mathbf{P_y} - \mathbf{P_y}\underline{\mathbf{J}})(\overline{\mathbf{J}}\mathbf{y} - \underline{\mathbf{J}} \ \mathbf{y})$$

$$= \mathbf{y}^{\mathrm{T}}(\mathbf{P_y}\overline{\mathbf{J}}\mathbf{y} - \mathbf{P_y}\underline{\mathbf{J}} \ \mathbf{y})$$

$$= \mathbf{y}^{\mathrm{T}}\mathbf{P_y}(\overline{\mathbf{J}} - \underline{\mathbf{J}}) \ \mathbf{y}, \quad (31)$$

and

$$\hat{\mathbf{g}}^{\mathrm{T}}\mathbf{P_y}\hat{\mathbf{g}} = (\mathbf{y} - \underline{\mathbf{J}} \ \mathbf{y})^{\mathrm{T}}\mathbf{P_y}(\mathbf{y} - \underline{\mathbf{J}} \ \mathbf{y})$$

$$= \mathbf{y}^{\mathrm{T}}(\mathbf{P_y} - \mathbf{P_y}\underline{\mathbf{J}})(\mathbf{y} - \underline{\mathbf{J}} \ \mathbf{y})$$

$$= \mathbf{y}^{\mathrm{T}}(\mathbf{P_y}\mathbf{y} - \mathbf{P_y}\underline{\mathbf{J}} \ \mathbf{y})$$

$$= \mathbf{y}^{\mathrm{T}}\mathbf{P_y}(\mathbf{I} - \underline{\mathbf{J}}) \ \mathbf{y}. \quad (32)$$

This proves that Eq. (7) is identical to Eq. (15).

References

[1] P. Vaníček, Approximate spectral analysis by least-squares fit, Astrophys. Space Sci. 4 (1969) 387–391.

[2] P. Vaníček, Further development and properties of the spectral analysis by least-squares, Astrophys. Space Sci. 12 (1) (1971) 10–33.

[3] S. Mallat, A Wavelet Tour of Signal Processing, vol. 637, Academic Press, Cambridge UK, 1999.

[4] D.E. Wells, P. Vaníček, S.D. Pagiatakis, Least-Squares Spectral Analysis Revisited, Department of Surveying Engineering, University of New Brunswick, Canada, 1985.

[5] M.R. Craymer, The Least-Squares Spectrum, Its Inverse Transform and Auto-correlation Function: Theory and Some Application in Geodesy (Ph.D. thesis), University of Toronto, Canada, 1998.

[6] S. Pagiatakis, Stochastic significance of peaks in the least-squares spectrum, J. Geod. 73 (2) (1999) 67–78.

[7] N.R. Lomb, Least-squares frequency analysis of unequally spaced data, Astrophys. Space Sci. 39 (2) (1976) 447–462.

[8] Y. Hui, S. Pagiatakis, Least squares spectral analysis and its application to superconducting gravimeter data analysis, Geo-Spat. Inf. Sci. 7 (4) (2004) 279–283.

[9] E. Ghaderpour, S.D. Pagiatakis, Q.K. Hassan, A survey on change detection and time series analysis with applications, Appl. Sci. 11 (13) (2021) 6141.

[10] E. Ghaderpour, S.D. Pagiatakis, Least-squares wavelet analysis of unequally spaced and non-stationary time series and its applications, Math. Geosci. 49 (7) (2017) 819–844.

[11] C. Torrence, G.P. Compo, A practical guide to wavelet analysis, Bull. Am. Meterol. Soc. 79 (1) (1998) 61–78.

[12] E. Ghaderpour, Least-Squares Wavelet Analysis and Its Applications in Geodesy and Geophysics (Ph.D. thesis), York University, Canada, 2018.

[13] E. Ghaderpour, S.D. Pagiatakis, LSWAVE: A MATLAB software for the least-squares wavelet and cross-wavelet analyses, GPS Solut. 23 (2) (2021) 50.

[14] E. Ghaderpour, JUST: MATLAB and python software for change detection and time series analysis, GPS Solut. 25 (3) (2021) 85.

[15] B. B., B. P., An efficient real-time implementation of the Wigner-Ville distribution, IEEE Trans. Acoust., Speech, Signal. Process. 35 (1987) 1611–1618.

[16] D. Waldo, P.R. Chitrapu, On the Wigner-Ville distribution of finite duration signals, Signal Process. 24 (1991) 231–237.

[17] Q. S., C. D., Discrete Gabor transform, IEEE Trans. Signal Process. 41 (7) (1993) 2429–2438.

[18] E. Sejdić, I. Djurović, J. Jiang, Time–frequency feature representation using energy concentration: An overview of recent advances, Digit. Signal Process. 19 (1) (2009) 153–183.

[19] R. Stockwell, L. Mansinha, R. Lowe, Localization of the complex spectrum: The S transform, IEEE Trans. Signal Process. 44 (1996) 998–1001.

[20] A. Moukadem, Z. Bouguila, D. Ould Abdeslam, A. Dieterlen, A new optimized Stockwell transform applied on synthetic and real non-stationary signals, Digit. Signal Process. 46 (2015) 226–238.

[21] G. Foster, Wavelet for period analysis of unevenly sampled time series, Astron. J. 112 (4) (1996) 1709–1729.

[22] A. Michel, A. Santamaría-Gómez, J.-P. Boy, F. Perosanz, S. Loyer, Analysis of GNSS displacements in Europe and their comparison with hydrological loading models, Remote Sens. 13 (22) (2021) 4523.

[23] D.A. Cucci, L. Voirol, G. Kermarrec, J.-P. Montillet, S. Guerrier, The generalized method of wavelet moments with eXogenous inputs: A fast approach for the analysis of GNSS position time series, J. Geod. 97 (2023) 14.

[24] J. Griffiths, J. Ray, Impacts of GNSS position offsets on global frame stability, Geophys. J. Int. 204 (1) (2016) 480–487.

[25] L. Crocetti, M. Schartner, B. Soja, Discontinuity detection in GNSS station coordinate time series using machine learning, Remote Sens. 13 (19) (2021) 3906.

[26] K. Chanard, L. Fleitout, E. Calais, P. Rebischung, J. Avouac, Toward a global horizontal and vertical elastic load deformation model derived from GRACE and GNSS station position time series, J. Geophys. Res.: Solid Earth 123 (2018) 3225–3237.

[27] A. Kaczmarek, B. Kontny, Identification of the noise model in the time series of GNSS stations coordinates using wavelet analysis, Remote Sens. 10 (10) (2018) 1611.

[28] K. Ji, Y. Shen, F. Wang, Signal extraction from GNSS position time series using weighted wavelet analysis, Remote Sens. 12 (6) (2020) 992.

[29] K. Ji, Y. Shen, Q. Chen, F. Wang, Extended singular spectrum analysis for processing incomplete heterogeneous geodetic time series, J. Geod. 97 (8) (2023) 74.

[30] A. Mao, C. Harrison, T. Dixon, Noise in GPS coordinate time series, J. Geophys. Res. 104 (B2) (1999) 2797–2816.

[31] S. Williams, Y. Bock, P. Fang, P. Jamason, R.M. Nikolaidis, L. Prawirodirdjo, M. Miller, D.J. Johnson, Error analysis of continuous GPS position time series, J. Geophys. Res.: Solid Earth 109 (B3) (2004) B03412.

[32] M. Bos, R. Fernandes, S. Williams, L. Bastos, Fast error analysis of continuous GNSS observations with missing data, J. Geod. 87 (4) (2013) 351–360.

[33] K. Chanard, M. Métois, P. Rebischung, J. Avouac, A warning against over-interpretation of seasonal signals measured by the Global Navigation Satellite System, Nature Commun. 11 (2020) 1375.

[34] C.R. Rao, S.K. Mitra, Generalized inverse of a matrix and its applications, Proceedings of the Sixth Berkeley Symposium on Mathematical Statistics and Probability, vol. 1 (1972) 601–620.

[35] R.R. Steeves, A statistical test for significance of peaks in the least-squares spectrum, in: Collected Papers of Geodetic Survey, Dept. of Energy, Mines and Resources, Surveys and Mapping, Ottawa, 1981, pp. 149–166.

[36] R.A. Horn, C.R. Johnson, Matrix Analysis, second ed., Cambridge University Press, 2012.

[37] A.T. Craig, R.V. Hogg, J. McKean, seventh ed., Introduction to Mathematical Statistics, vol. 694, Pearson, 2013.

[38] J. Morlet, Sampling theory and wave propagation, in: C. Chen (Ed.), Issues in Acoustic Signal–Image Processing and Recognition, in: NATO ASI Series (Series F: Computer and System Sciences), vol. 1, 1983, pp. 233–261.

[39] E. Ghaderpour, C. Masciulli, M. Zocchi, R. Marini, G. Mastrantoni, F. Reame, G. Pantozzi, N. Belcecchi, G. Scarascia Mugnozza, P. Mazzanti, Least-squares wavelet analysis of rainfalls and landslide displacement time series derived by PS-InSAR, in: O. Valenzuela, F. Rojas, L.J. Herrera, H. Pomares, I. Rojas (Eds.), Theory and Applications of Time Series Analysis, Springer Nature Switzerland, Cham, 2023, pp. 117–132.

[40] E. Ghaderpour, Least-squares wavelet and cross-wavelet analyses of VLBI baseline length and temperature time series: Fortaleza–Hartebeesthoek–Westford–Wettzell, Publ. Astron. Soc. Pac. 133 (1019) (2021) 014502.

[41] L. Tunini, A. Magrin, G. Rossi, D. Zuliani, Global Navigation Satellite System (GNSS) time series and velocities about a slowly convergent margin processed on high-performance computing (HPC) clusters: Products and robustness evaluation, Earth Syst. Sci. Data 16 (2) (2024) 1083–1106.

[42] C. Fidani, The central Italy electromagnetic network and the 2009 L'Aquila earthquake: Observed electric activity, Geosciences 1 (1) (2011) 3–25.

[43] P.M. Barone, R.M. Di Maggio, Forensic investigations of geohazards: The Norcia 2016 earthquake, Geosciences 8 (9) (2018) 316.

[44] M. Crosetto, O. Monserrat, M. Cuevas-González, N. Devanthéry, B. Crippa, Persistent scatterer interferometry: A review, ISPRS J. Photogramm. Remote Sens. 115 (2016) 78–89.

[45] S. Moretto, F. Bozzano, P. Mazzanti, The role of satellite InSAR for landslide forecasting: Limitations and openings, Remote Sens. 13 (2021) 3735.

[46] A. Vradi, J. Sala, L. Solari, J. Balasis-Levinsen, Validating the European Ground Motion Service: An assessment of measurement point density, in: The International Archives of the Photogrammetry, Remote Sensing and Spatial Information Sciences, vol. XLVIII-4/W7-2023, Elsevier, 2023, pp. 247–252.

[47] M.R. Ahmed, E. Ghaderpour, A. Gupta, A. Dewan, Q.K. Hassan, Opportunities and challenges of spaceborne sensors in delineating land surface temperature trends: A review, IEEE Sens. J. 23 (7) (2023) 6460–6472.

[48] E. Ghaderpour, E. Ince, S. Pagiatakis, Least-squares cross-wavelet analysis and its applications in geophysical time series, J. Geod. 92 (2018) 1223–1236.

[49] A. Santamaría-Gómez, M.-N. Bouin, X. Collilieux, G. Wöppelmann, Correlated errors in GPS position time series: Implications for velocity estimates, J. Geophys. Res.: Solid Earth 116 (B1) (2011).

[50] J. Zhang, Y. Bock, H. Johnson, P. Fang, S. Williams, J. Genrich, S. Wdowinski, J. Behr, Southern California permanent GPS geodetic array: Error analysis of daily position estimates and site velocities, J. Geophys. Res.: Solid Earth 102 (B8) (1997) 18035–18055.

[51] C. Benoist, X. Collilieux, P. Rebischung, Z. Altamimi, O. Jamet, L. Métivier, K. Chanard, L. Bel, Accounting for spatiotemporal correlations of GNSS coordinate time series to estimate station velocities, J. Geodyn. 135 (2020) 101693.

[52] B. Yang, Z. Yang, Z. Tian, P. Liang, Weakening the flicker noise in GPS vertical coordinate time series using hybrid approaches, Remote Sens. 15 (2023) 1716.

[53] P. Rebischung, K. Chanard, L. Metivier, Z. Altamimi, Flicker noise in GNSS station position time series: How much is due to crustal loading deformations? in: AGU Fall Meeting Abstracts, vol. 2017, 2017, pp. G13A–04.

[54] M. Rajner, T. Liwosz, Analysis of seasonal position variation for selected GNSS sites in Poland using loading modelling and GRACE data, Geod. Geodyn. 8 (4) (2017) 253–259.